1 **Title: Immune Signatures of SARS-CoV-2 Infection Resolution in Human Lung Tissues**

2

3 **Short Title: SARS-CoV-2 infection resolution in human lung tissues**

4

5 **One sentence summary:** We comprehensively mapped the human immunological dynamics

6 associated with successful resolution of SARS-CoV-2 infection in human lung tissues.

7

8 Devin Kenney[1,2], Aoife K. O'Connell[1,2,4], Anna E. Tseng[1,2,4], Jacquelyn Turcinovic[1,2,3], Maegan L.

9 Sheehan[7,12], Adam D. Nitido[7,12], Paige Montanaro[2,4], Hans P. Gertje[2,4], Maria Ericsson[6], John H.

10 Connor[1,2], Vladimir Vrbanac[7], Nicholas A. Crossland[1,2,4], Christelle Harly[8,9,12]*, Alejandro B.

11 Balazs[7,12]*, and Florian Douam[1,2,12,13] *

12

13 [1]Department of Virology, Immunology, and Microbiology, Boston University Chobanian &

14 Avedisian School of Medicine, Boston, MA, USA.

15 [2] National Emerging Infectious Diseases Laboratories, Boston University, Boston, MA, USA.

16 [3] Bioinformatics Program, Boston University, Boston, MA, USA.

17 [4] Department of Pathology and Laboratory Medicine, Boston University Chobanian & Avedisian

18 School of Medicine, Boston, MA, USA.

19 [6] Electron Microscopy Core Facility, Harvard Medical School, Boston, MA, USA.

20 [7] Ragon Institute of MGH, MIT and Harvard, Cambridge, MA, USA.

21 [8] Université de Nantes, INSERM, CNRS, CRCINA, Nantes, France

22 [9] LabEx IGO 'Immunotherapy, Graft, Oncology', Nantes, France.

23 [12] These authors contributed equally to the work.

24 [13] Lead contact

25 *Correspondence:

26   Florian Douam, National Emerging Infectious Diseases Laboratories, 620 Albany Street Boston

27   MA 02118 USA, +1-617-358-9174, fdouam@bu.edu.

28   Alejandro B. Balazs, Ragon Institute of MGH Harvard and MIT, 400 Technology Square

29   Cambridge MA 02139 USA, +1-857-268-7197, abalazs@mgh.harvard.edu.

30   Christelle Harly, CRCINA - Institut de Recherche en Santé de Nantes Université, 8 quai

31   Moncousu 44 007 Nantes France, +33-2 28 08 02 08, christelle.harly@inserm.fr.

32

33   The authors have declared that no conflict of interest exists.

34

35

36

37

38

39

40

41

42

43

44

45

46

47

48

49

50

51

ABSTRACT

While human autopsy samples have provided insights into pulmonary immune mechanisms associated with severe viral respiratory diseases, the mechanisms that contribute to a clinically favorable resolution of viral respiratory infections remain unclear due to the lack of proper experimental systems. Using mice co-engrafted with a genetically matched human immune system and fetal lung xenograft (fLX), we mapped the immunological events defining successful resolution of SARS-CoV-2 infection in human lung tissues. Viral infection is rapidly cleared from fLX following a peak of viral replication, histopathological manifestations of lung disease and loss of AT2 program, as reported in human COVID-19 patients. Infection resolution is associated with the activation of a limited number of hematopoietic subsets, including inflammatory monocytes and non-canonical double-negative T-cells with cytotoxic functions, which are highly enriched in viral RNA and dissipate upon infection resolution. Activation of specific human fibroblast and endothelial subsets also elicit robust antiviral and monocyte chemotaxis signatures, respectively. Notably, systemic depletion of human CD4+ cells, but not CD3+ cells, abrogates infection resolution in fLX and induces persistent infection, supporting evidence that peripheral CD4+ monocytes are important contributors to SARS-CoV-2 infection resolution in lung tissues. Collectively, our findings unravel a comprehensive picture of the immunological events defining effective resolution of SARS-CoV-2 infection in human lung tissues, revealing markedly divergent immunological trajectories between resolving and fatal COVID-19 cases.

INTRODUCTION

Coronavirus disease 2019 (COVID-19) is a respiratory disease that has swept the world since its emergence in the Wuhan province of China in late 2019. The etiologic agent of COVID-19, the Severe Acute Respiratory Syndrome Coronavirus 2 (SARS-CoV-2) is a plus-sense, enveloped RNA virus that targets the epithelium of the respiratory tract. Infection results in varying severities of COVID-19, with most cases being mild to asymptomatic. The onset of severe disease is associated with aberrant immune responses (e.g., excessive pulmonary infiltration of myeloid cells, inflammasome-activated monocytic cells, macrophage exacerbated inflammation) and severe lung injury (e.g., lung consolidation, diffuse alveolar damage (DAD), and thrombosis) (*1-9*).

A large number of human studies have been instrumental in unraveling cellular and molecular processes driving severe COVID-19 disease in infected tissues, particularly in the respiratory tract, using autopsy samples (*10-13*). In parallel, human studies of resolving COVID-19, including controlled human challenge studies, have leveraged peripheral blood and nasopharyngeal samples to identify human signatures of effective infection resolution and mild disease (*14-16*). Notably, this includes individuals with specific HLA haplotypes (*15*), evidence of previous coronavirus exposure (*15, 17, 18*), rapid nasopharyngeal immune infiltration (*14*), and non-productive infection of nasopharyngeal T-cells and macrophages (*14*). However, tissue-specific human immunological processes associated with protection, such as extravasation of recruited immune lineages and their differentiation processes, have remained elusive due to the ethical considerations associated with tissue sampling of individuals with mild disease and human challenge models. Although large and small animal models of COVID-19 are available, the high-cost and limited reagent availability associated with non-human primate models, and the large divergence between rodent and human immune systems (*19, 20*) further underscore the need for additional models capable of recapitulating human protective immune responses to SARS-CoV-2 infection.

4

104   Mice engrafted with human fetal lung xenograft (fLX) support infection by multiple human

105   respiratory viruses, including human cytomegalovirus (HCMV), Middle East respiratory syndrome

106   coronavirus (MERS-CoV) and SARS-CoV-2 (21-23). Upon co-engraftment with a human immune

107   system (HIS), these animals also mount lung-resident human immune responses against these

108   pathogens (21, 23-25). Recently, our group reported that mice engrafted with fLX are highly

109   susceptible to SARS-CoV-2 infection and lung tissue damage and support persistent viral

110   infection (23). However, co-engraftment of fLX and HIS in a xenorecipient strain supporting

111   enhanced myelopoiesis (i.e., HNFL mouse model) rapidly blunted viral infection and prevented

112   widespread acute viral replication across fLX, resulting in protection from histopathology of fLX

113   (23). Our findings unraveled a human macrophage antiviral signature as a correlate of such rapid

114   protection against SARS-CoV-2 infection. However, how the human immune system mobilizes

115   and resolves infection upon extensive viral replication within human lung tissues, a context that

116   more likely describes mild cases of SARS-CoV-2 infection, has remained elusive.

117   In this study, we leverage previously described immunodeficient mice engrafted with a

118   human fetal lung xenograft (fLX) and a genetically matched human immune system, fetal liver

119   and thymus (BLT-L mice) (21) to conduct the first comprehensive mapping of human

120   immunological correlates of resolution of acute SARS-CoV-2 infection in human lung tissues.

121   Consistent with previous reports (24, 25), BLT-L mice are permissive to SARS-CoV-2 infection

122   following direct viral inoculation into the fLX. Infection swiftly resolves by 6 days post-infection

123   (dpi) following an early viral replication peak at 2 dpi. Acute viral infection is associated with lung

124   histopathological damage and loss of AT2 program, as described in COVID-19 patients (1).

125   Notably, acute infection is also defined by the emergence of a limited set of hyper-activated

126   hematopoietic subsets, including inflammatory monocytes and T-cells expressing genes

127   canonically found in macrophages. Of these, inflammatory monocytes appear to mount the most

128   robust antiviral responses and are highly enriched in viral RNA before phasing out from the tissues

129   after resolution. No inflammasome activation in these cells was observed despite enrichment in

130 viral RNA. This contrasts with reports from fatal COVID-19 cases (*26*) and evidence suggesting

131 that monocyte and macrophage infections in vitro and in vivo are associated with inflammasome

132 activation (*27, 28*).

133 Specific fibroblast and endothelial cell subsets also contribute to antiviral responses and

134 hematopoietic chemotaxis, respectively, underscoring how crosstalk between hematopoietic and

135 non-hematopoietic lineages likely contributes to infection resolution. At 12 dpi, the immune

136 landscape in fLX is characterized by an increase in CD4+ patrolling monocytes, conventional

137 dendritic cells and CD206+ interstitial macrophages (IM). Notably, systemic depletion of human

138 CD4+ cells, but not human CD3+ cells, abrogates SARS-CoV-2 clearance in fLX and causes

139 persistent infection. These findings underscore CD4+ circulating monocyte infiltration as a likely

140 feature that defines SARS-CoV-2 infection resolution.

141 Collectively, our work sheds light on a unique set of immunological events associated with

142 SARS-CoV-2 resolution in human lung tissues which dramatically contrasts with the immune

143 trajectories reported in fatal COVID-19 cases. This work opens avenues for mechanistically

144 dissecting the respective contributions of the hematopoietic and non-hematopoietic subsets

145 identified in this study, which could inform the development of immunotherapies against viral

146 respiratory diseases.

147

148 **RESULTS**

149 **BLT-L mice effectively clear SARS-CoV-2 infection following acute viral replication**

150 Previous work from our laboratory (*23*) and others (*21, 24, 25*) have shown that

151 immunodeficient mice can successfully be engrafted with human fetal lung xenograft (fLX) alone

152 or in combination with a human immune system (HIS). In this study, we leveraged a previously

153 reported mouse model co-engrafted with fetal liver and thymus as well as with human

154 hematopoietic stem cells (HSC) and fLX (BLT-L mice) (*21*). Fetal liver and thymus were engrafted

155 under the renal capsule of adult NOD.Cg-*Prkdc^{scid} Il2rg^{tm1Wjl}*/SzJ (NSG) mice (12-16 weeks old)

156   prior to intravenous HSC injection. A piece of fetal lung tissue was subcutaneously engrafted on

157   the flank of each animal, as described previously (*21*) (**Fig. 1A**). To determine the susceptibility

158   of BLT-L mice to SARS-CoV-2 infection and their ability to effectively clear infection, BLT-L mice

159   were inoculated with SARS-CoV-2 (2019-nCoV/USA_WA1/2020) via intra-graft injection. We

160   used a viral dose (10^6 PFU) that we previously established to drive robust and persistent infection

161   in fLX of immunodeficient mice not engrafted with a HIS (*23*) (**Fig. 1B**).

162   Throughout the course of infection, mice did not display any weight loss (**Fig. 1C)** or

163   clinical signs of disease such as lethargy or lack of responsiveness (data not shown). To assess

164   lung histopathology and viral titers longitudinally, fLX were collected at 2, 6, and 12 dpi. Plaque

165   assay was performed on fLX homogenates to determine viral titers. A significant amount of

166   infectious viral particles could be recovered from fLX at 2 dpi (3.20 ± 2.52 log([PFU/mg of tissue]),

167   but not at 6dpi (0.281 ± 0.688 log[PFU/mg of tissue]) and 12 dpi (0.111 ± 0.293 log[PFU/mg of

168   tissue]) (**Fig. 1D**). These data demonstrated a peak of viral infection at 2 dpi, prior to resolution of

169   infection by 6 dpi. Immunohistochemistry (IHC) for SARS-CoV-2 Spike (S) protein revealed

170   infection was mainly found in the alveolar epithelium of fLX at 2 dpi (**Fig. 1E,F**). Consistent with

171   viral quantification, most viral antigen was cleared by 6 dpi and became undetectable by 12 dpi

172   (**Fig.1G,H**). SARS-CoV-2 S was primarily detected in the alveolar and bronchiole epithelium along

173   with necrotic cellular debris, consistent with the primary cell targets of SARS-CoV-2 (**Fig.1E**).

174   These findings were confirmed through IHC for SARS-CoV-2 nucleoprotein (N) at 2, 6 and 12 dpi

175   (**Fig. 1I-L**) and transmission electron microscopy (TEM) imaging of fLX at 2 dpi (**Fig. S1A-C**).

176   Notably, TEM substantiated evidence of productive fLX infection, as indicated by the presence of

177   viral particles in the cytosol of epithelial cells and budding/invagination of virions (**Fig. S1A-C**).

178   Next, we examined histopathological phenotypes associated with active and resolved

179   infection. Interpretation of hematoxylin and eosin (H&E) staining illustrated denuding of

180   pneumocytes, neutrophil infiltration, edema, hemorrhage, thrombosis, and pneumocyte necrosis,

181   which correlated with sites of infection at 2 dpi (**Fig. 2A-E**). No major signs of histopathological

182   lung damage were observed at 6 and 12 dpi compared to naïve fLX, indicating that fLX can mount

183   repair mechanisms upon resolution of infection (**Fig. 2F-G**). A previously described semi-

184   quantitative histopathological scoring system (*23*) provided statistical confirmation for a significant

185   increase in lung pathology at 2 dpi, which was no longer apparent at 6 (**Fig. 1H**) or 12 dpi. Of

186   note, minor lung pathology was observed at baseline (naïve), likely reflecting limited graft vs. host

187   disease. Together, infection of fLX of BLT-L mice recapitulates many important hallmarks of acute

188   SARS-CoV-2 infection, including viral replication and histopathological manifestations of disease,

189   prior to effective viral clearance and lung tissue repair.

190

191   **Humoral responses do not drive SARS-CoV-2 clearance in BLT-L mice despite evidence of**

192   **Spike selective pressure.**

193   We first asked whether SARS-CoV-2 infection resolution was driven by human

194   neutralizing humoral responses. Consistent with the rapid clearance of infectious viral particles

195   by 6 dpi and the known caveat that humanized mice mount limited humoral responses (29), there

196   were no detectable neutralizing antibodies in serum collected at 2 or 12 dpi (**Fig. S2A, B**).

197   However, interestingly, genomic sequencing of virus isolated from fLX at 2 dpi revealed the

198   selection of two stable mutations in 75% of fLX (**Fig. S2C**, **Table S1**). Both mutations were located

199   in the Spike N-terminal domain (NTD): an insertion (216KLRS) and a non-synonymous mutation

200   (R245H), neither of which were present in the inoculum (**Fig. S2C**, **Table S1**). Interestingly, these

201   two mutations were found together in 100% of the viral sequences, suggesting potential co-

202   evolution (**Fig. S2D**). They have also been reported as positively selected in the context of sub-

203   optimal neutralizing antibody concentration (216KLRS) (*29*) or the context of cross-species

204   adaptation (216KLRS and R245H) (*30*). Despite lacking humoral responses, these findings reveal

205   that BLT-L mice can recapitulate host-pathogen interactions that drive SARS-CoV-2 evolution

206   and host adaptation.

207

8

SARS-CoV-2 infection remodels the human lung cellular environment.

To comprehensively map the fLX responses associated with resolution of SARS-CoV-2 infection, we performed single-cell RNA sequencing (scRNA-seq) on fLX from naïve BLT-L mice and at 2 and 12 dpi. While most cells detected in fLX by scRNA-seq were human, a minor population of mouse cells was detected, which were excluded from downstream analysis (**Fig. S3A-C**). Initial analysis of the human compartment revealed diverse hematopoietic (T-cells/innate lymphoid cells (ILC), B cells, myeloid cells and mast cells) and non-hematopoietic lineages (ciliated and non-ciliated epithelial, endothelial, mesenchymal cells and chondrocytes) in both naïve and infected fLX (**Fig. 3A-C and Fig. S3D,E**).

T-cells and innate lymphoid cells (ILC) have the same transcriptional programs, express TCR genes, and play similar effector functions (*31*). Their shared features render them very challenging to distinguish by scRNAseq in small datasets and without TCR sequencing information (*32*). We thus considered them together as part of a T-cell/ILC population. T-cell/ILC frequency dramatically decreased in fLX upon infection (naïve, 66.8%; 2 dpi, 35.3%; 12 dpi, 21.8%), which is consistent with evidence that COVID-19 can induce lymphoid depletion(*33, 34*) (**Fig. 3B,C**). Notably, lymphopenia was not observed in the peripheral blood of BLT-L mice, suggesting lymphocyte depletion in fLX was not directly attributed to declining circulating peripheral lymphocytes (**Fig. S3F**). In contrast, myeloid (naïve, 9.94%; 2 dpi, 25.3%; 12 dpi, 22.2%) and B-cell subsets (naïve, 3.64%; 2 dpi, 5.38%; 12 dpi, 5.31%) relatively expanded upon infection (**Fig. 3B,C**). The epithelial, endothelial and mesenchymal cell frequencies increased upon infection, while mast cell, ciliated cell and chondrocyte frequencies decreased (**Fig. 3B,C**). Notably, most human clusters showed temporal segregation between naïve fLX and fLX at 2 and 12 dpi (**Fig. 3B and Fig. S3E**; naïve: black subclusters; 2 dpi: red subclusters and 12 dpi: blue subclusters). This suggests that infection alters the transcriptional state of many cell types and/or drives the emergence of novel cell subsets. Notably, acute infection at 2 dpi led to the emergence of distinct T, myeloid, and mesenchymal cell populations, labeled as subclusters A, B, and C,

234 respectively (**Fig. 3B**). Resolved infection (12 dpi) was associated with the emergence of

235 transcriptomically distinct epithelial, endothelial, mesenchymal, B-cell and myeloid subclusters;

236 while we did not observe the emergence of transcriptomically divergent subclusters within the T-

237 cell lineages at that time point. Temporal separation of several human lineages suggests a two-

238 step tissue remodeling process during infection involving i) an initial antiviral phase mediated by

239 a limited set of human subpopulations and ii) a tissue repair phase involving a broader range of

240 human subpopulations.

241 Next, we wished to utilize scRNAseq to determine the cellular compartments enriched in

242 viral RNA. We found that viral RNA was mainly within three major lineages: mesenchymal, T-

243 cell/ILCs and myeloid (**Fig.4A,B**). AT2 and the overall epithelial compartment were not

244 significantly enriched in viral RNA despite histological evidence of epithelial infection in fLX at 2

245 dpi (**Fig. 4A and 1F,J**). Previous evidence that SARS-CoV-2 induces significant cytopathic

246 damage in AT2 cells (*35*) may suggest that infected AT2 cells are lost when undergoing the

247 scRNAseq pipeline. Within the mesenchymal cluster, viral reads were limited and distributed

248 sporadically without significant enrichment within a given subcluster (**Fig. 4B,C**). However, viral

249 RNA was strongly enriched within the 2 dpi-specific populations in the myeloid and T-cell clusters,

250 previously labeled as clusters A and B (**Fig. 4A,B**), warranting further investigations.

251

252 **Human lung epithelium signatures upon SARS-CoV-2 infection recapitulate features of**

253 **COVID-19.**

254 Subclustering of the human epithelial compartment revealed subclusters of airway basal

255 and secretory cells, alveolar type 1 (AT1) and type 2 (AT2) cells, and serous cells (**Fig. 5A**). The

256 dynamic changes of the epithelial compartment upon infection were consistent with COVID19

257 human studies (*2, 5, 36*). We noted a relative reduction of the AT2 compartment at 2 dpi (25.6%)

258 compared to naïve mice (73.1%). The AT2 compartment was partially restored at 12 dpi (49.1%)

259 (**Fig. 5B**). The frequency of basal airway cells followed a reversed trend, indirectly reflecting the

10

260   disruption of the AT2 compartment. The size of the AT1 compartment showed a relative increase

261   at 2 dpi (9.89% compared to 8.00% in naïve fLX), consistently with the ability of AT2 cells to

262   differentiate into AT1 upon lung damage (*37*) before returning to minimal relative levels as the

263   AT2 compartment re-expanded following infection resolution.

264   The AT2 compartment displayed the most robust remodeling upon viral infection across

265   the entire epithelial compartment, with 2 dpi and 12 dpi AT2 subclusters showing distinctive

266   transcriptomic signatures compared to naïve AT2 cells (**Fig. 5C**). Interestingly, AT2 cells did not

267   exhibit robust antiviral responses upon acute infection (**Fig. 5C**). However, they displayed gene

268   signatures previously reported during and after SARS-CoV-2 infection including, downregulation

269   of MHC genes (*HLA-C, HLA-B, and HLA-DPB1)* and *CCL5* (a cytokine associated with immune

270   recruitment during respiratory infection) (*6*), upregulation of immunomodulatory genes regulating

271   inflammation and cell stress (*SFTPA1*, *EGR1*), and elevated expression of genes associated with

272   mitochondrial dysfunctions and increased oxidative stress responses (i.e., *LARS2*). (**Fig. 5C**).

273   Activation of tissue repair mechanism (*SNHG8*) was also observed, further underscoring evidence

274   of physiologically relevant AT2 response to viral infection (**Fig. 5C**). The absence of detectable

275   viral RNA in AT2 cells was in line with the lack of antiviral responses. Such a lack of infected AT2

276   cells in our scRNAseq data is likely the reflection of their vulnerability and death during infection,

277   given histological evidence of epithelial infection (**Fig. 1F, J**) and the marked reduction of the AT2

278   compartment in fLX upon infection (**Fig. 5B**).

279   Collectively, the epithelial compartment of fLX of BLT-L mice recapitulates several

280   previously reported features of COVID-19 in humans, including loss of AT2 program,

281   downregulation of immune genes and antigen presentation, and activation of tissue repair

282   mechanisms.

283

284   **SARS-CoV-2 infection resolution is associated with the emergence of a viral RNA-enriched**

285   **double-negative T-cell subcluster with cytotoxic functions.**

11

286   We first aimed to characterize the T-cell signatures to SARS-CoV-2 infection resolution,

287   and with that, the features of our viral RNA-enriched, 2 dpi-specific, T-cell/ILC subcluster A. T-

288   cell/ILC responses to infection were mainly limited to this specific viral RNA-associated subcluster

289   (**Fig. 6A-D**), which segregated very distinctively from other CD3+ T-cell lineages, including

290   canonical CD4+ and CD8+ T-cells (Subcluster 6; **Fig. 6A-C**). Using doublet discriminators and

291   assessing viral RNA abundance; we determined that this subcluster was not a doublet and

292   displayed low levels of *CD4* and *CD8* transcripts, suggesting a double-negative profile, and

293   elevated levels of mitochondrial transcripts **(Fig. S4A,B)**. Most notably, it was uniquely defined

294   by the expression of several transcripts known to be enriched in macrophages (*MARCO*, *TIMP1*,

295   *LYZ*), fibroblasts (*MGP*, *CALD1*, *COL1A*), or both (*A2M*, *IFITM3*) but not in T-cells (**Fig. 6E and**

296   **Fig. S4C**). This subcluster also exhibited evidence of cytotoxic function through the expression of

297   *GZMA*, *GZMB*, and *GNLY* transcripts, albeit expression was also detected in CD8+ T-cells and

298   activated tissue-resident memory T-cells (TRM) (Subclusters 1,3,4, **Fig. 6E**). Notably, a

299   subpopulation of double-negative T-cells sharing some of these cytotoxic markers has been

300   previously reported in mouse spleen(*38*). Given the proximity of this subcluster with myeloid

301   lineages (**Fig. 3A,B**) and evidence of expression of macrophage-enriched transcripts, we referred

302   to this subcluster as myeloid-like double-negative T-cells (mDNT cells). mDNT cells also exhibited

303   upregulation of key gene pathways related to COVID-19, SARS-CoV-2 cell-intrinsic immune

304   responses, cellular cytotoxicity (e.g., degranulation) and cell death, consistently with a role for this

305   subset to serve as a robust primary responder to viral infection (**Fig. 6D**). Of note, a recent human

306   challenge study reported that self-resolving SARS-CoV-2 infection is associated with non-

307   productive infection of human nasopharyngeal T-cells(*14*). In contrast, in lung autopsy samples

308   of fatal COVID-19 cases, viral RNA was enriched in myeloid cells but was not detected in T-

309   cells(*39*). Collectively, our findings underscore that the emergence of viral RNA-enriched T cell

310   populations displaying myeloid-like features in infected lung tissues is associated with effective

311   SARS-CoV-2 infection resolution.

312

Transient antiviral responses by a viral RNA-enriched inflammatory monocyte subset define lung myeloid responses driving SARS-CoV-2 infection resolution.

Sub-clustering of myeloid lineages unveiled diverse subpopulations, including alveolar and macrophages (AM) and IM, various monocyte subsets, and one conventional DC subset (cDC) (**Fig. 7A and Fig. S5A-C**). Across all time points, monocytes represented the largest sublineage, which was divided into three subgroups: naïve/resting, patrolling intravascular monocytes (PIM), and inflammatory monocytes (iMO). iMO and AM were the only two subclusters increasing in frequencies upon acute infection at the relative expense of cDC and IM (**Fig.7B,C**). An increase in frequencies within these subclusters was associated with the emergence of distinctive iMO and AM cell populations with infection-induced transcriptomic signatures, underscoring a direct response of these subclusters against viral infection. Following infection resolution, most iMO had phased out and frequencies of alveolar macrophages were concomitantly reduced. Conjointly, the relative number of IM, cDCs and PIM increased through the recruitment of cell populations with distinctive transcriptomic identities from naïve and infection-associated cell populations (**Fig. 7B**, blue).

Despite the moderate expansion of AM at 2 dpi, iMO were the most abundant myeloid lineage at 2 dpi (33.5%; **Fig. 7B, C**) and uniquely defined among other monocyte subclusters through elevated expression of *VCAN, S100A8, CD14, CD163* and absence/minimal expression of *CD4, MARCO and CD206 (MRC1)* (**Fig. 7D-F and Fig. S5D**). iMO were also the leading mediators of antiviral responses across all other myeloid subclusters, as exemplified by the robust upregulated expression of interferon-stimulated genes (ISGs) and inflammatory cytokines (*CCL8, CXCL10, CCL2, ISG15, DEFB1, IL1RN, IFIT1, ISG20, IFIT3,* and *MX1*), as well as inflammatory markers such as *CD163* (**Fig. 7E,G**). While some ISGs (e.g., *ISG15, IFIT3, and MX1*) were expressed in other myeloid lineages at 2 dpi, their expression was markedly lower compared to iMO. Notably, upregulation of *CCL8*, *CXCL11* and *DEFB1* transcripts were the most exclusive to

13

338 iMO (**Fig. 7G**). iMO were also highly enriched in viral RNA, and corresponded to the previously

339 referred 2 dpi-specific viral RNA-enriched subcluster B (**Fig. 3B, 4B, and 7A,B,H**), which also

340 suggested an association between enrichment in viral RNA and potentiated antiviral responses.

341 Concomitantly, we examined whether viral RNA-associated iMOs (CoV-iMOs) displayed a

342 specific transcriptomic signature compared to iMOs (noCoV-iMOs) with undetectable viral RNA.

343 Notably, only two genes correlated with the presence of viral RNA in iMOs: *FGL2 and C15orf48*

344 (**Fig. 7I**). While *FGL2* was down-regulated in CoV-iMO compared to noCoV-iMOs, *C15orf48* was

345 upregulated (**Fig. 7I**). Soluble FGL2 exerts immunosuppressive functions (notably by inhibiting

346 the NF-kB pathway) (*40*). Conversely, the mitochondrial protein C15orf48 is positively regulated

347 by NF-kB signaling (*41*) and has previously been implicated in severe COVID-19, acting as a

348 positive regulator of inflammation (*42*). A recurring feature of lung monocytes in fatal cases of

349 COVID-19 is the expression of *IL-1β* (*1, 2, 6-8*), and inflammasome activation has been

350 associated with the non-productive infection of monocytes(*27*). However, no *IL-1β* expression or

351 inflammasome activation was detected in CoV-iMOs despite enrichment in viral RNA.

352 In contrast to iMO, *CD4+ CD163- CD206(MRC1)*-PIM were detectable at all time points

353 (**Sub-cluster 0**; **Fig. 7 A-C**). 2 dpi-specific PIM harbored a distinctive, intermediate transcriptomic

354 signature bridging naïve PIM and 2 dpi-specific iMO, and that was defined by the upregulation of

355 specific interferon-stimulated genes (ISGs) such as *IFI27 and XAF1*, and pro-inflammatory genes

356 (*S100A11*) (**Fig. 7J**). At 12 dpi, PIM was the dominant subset over other monocyte subsets

357 (50.3%; **Fig. 7C**) and displayed a unique transcriptomic profile associated with anti-inflammation,

358 tissue repair and cellular debris clearance mechanisms, notably through the upregulation of

359 *FGL2, DYNLL1* and *CX3CR1*. At 12 dpi, expanded cDC and IM populations also elicited

360 comparable transcriptomic signatures.

361 mIHC analysis supported our scRNA seq findings. We observed a significant increase in

362 CD4- CD3- CD163+ cells in fLX in the extravascular interstitium and alveolar spaces, mirroring

363 the 2 dpi-specific expansion of CD4- CD163+ iMO and alveolar macrophages uncovered through

14

364   scRNA seq (**Fig. 7K**). CD3- CD4+ CD163- at that time point could be associated with the 2 dpi-

365   specific PIM population infiltrating the infected fLX. mIHC also recapitulated the reduction of CD3+

366   T-cells (**Fig. 7K**) at 2 dpi. At 12 dpi, fLX were still enriched in CD4+ cells, likely reflecting PIM

367   infiltration (**Fig. 7K**). CD163+ cells also persisted in fLX at 12 dpi, which can be explained by the

368   combined expansion of IM (CD4+ CD163+) and presence of AM (CD4- CD163+) at that time point

369   as CD163+ iMO phase out (**Fig. 7K**).

370   Collectively, our findings underscore a coordinated myeloid mobilization to infection

371   resolution and tissue repair, with iMO concentrating viral materials and robust antiviral responses.

372   As the viral materials are resolved, iMO populations dissipate, opening niches for other myeloid

373   lineages to engage in a coordinated tissue repair process.

374

375   **Mesenchymal and endothelial signatures of infection resolution**

376   We then examined the contribution of the mesenchymal and endothelial compartment in

377   mediating effective infection resolution. Relative expansion of the mesenchymal compartment

378   upon infection was mainly driven by an increase in fibroblast populations (**Fig. 3C; Fig. 8A,B**). An

379   increase in alveolar fibroblasts was observed at 12 dpi (49.6%; naïve=28.1%), which was

380   preceded by the emergence of a 2 dpi-specific cluster of activated fibroblasts (26.5%;

381   naïve=8.9%) (**Fig. 8A-C**), consistent with effective tissue repair in response to lung damage.

382   Activated fibroblasts were the dominant mesenchymal population in mediating antiviral responses

383   (**Fig. 8D**), as displayed by robust upregulation of major pro-inflammatory mediators such as

384   *CXCL10* and *TIMP1* (**Fig. 8F**).

385   The endothelial compartment is an important modulator of immune recruitment through

386   cytokine/chemokine signaling. Infected fLX showed the emergence of an activated, 2 dpi-specific

387   endothelial cell cluster (**Fig. 8G,H**), which was identified by increased expression of several

388   transcripts involved in myeloid chemotaxis (**Fig. 8I**), including *CXCR4* and *MCAM* (*43, 44*).

389   Notably, venous endothelial cells also displayed upregulation of a panel of interferon-stimulated

390   gene transcripts (*XAF1, IFIT1, MX1, IFI44L, RSAD2)* at 2 dpi (**Fig. 8J**) and the downregulation of

391   several transcripts coding for activation markers (*CD69*), MHC genes (*HLA-DPB1, HLA-C*) and

392   major proteins regulating cellular metabolism and transcription (*HSP90AA1, RPL13A*), which was

393   reflective of endothelial dysfunction and stress (**Fig. 8J**) consistently with human patient reports

394   and animal studies (*45-48*). Collectively, our findings support the contribution of the mesenchymal

395   and endothelium compartments in driving antiviral responses and myeloid chemotaxis,

396   respectively, in driving infection resolution.

397

398   **Systemic depletion of CD4+ cells abrogates viral clearance in fLX.**

399   Many of our findings underscore a robust association between monocyte recruitment into

400   fLX and SARS-CoV-2 infection resolution. This includes: 1) the recruitment of CD4+ PIM into

401   infected fLX, 2) the monocyte nature of iMO and of their dominant antiviral responses, 3) the high

402   enrichment in viral RNA of iMO during infection and 4) the endothelial-mediated myeloid

403   chemotaxis signature at 2 dpi. These pieces of evidence also complement recent human findings

404   which associate effective control of SARS-CoV-2 infection in the nasopharynx with monocyte

405   recruitment(*14*). Antibody-mediated depletions are commonly used to deplete specific

406   hematopoietic subsets, and they are particularly amenable to HIS mouse model studies; further

407   emphasizing the power of these *in vivo* platforms to mechanistically dissect immunological

408   mechanisms in a human context. However, no anti-human CD14 antibodies have been well

409   characterized for *in vivo* depletion of human monocytes. In contrast, anti-human CD4 antibodies

410   have been. To experimentally validate the importance of the recruitment of circulating monocytes

411   to drive infection resolution in fLX, we therefore performed systemic depletion of CD3+, CD4+,

412   and CD8+ cells through the administration of OKT3, OKT4, or OKT8 depleting antibodies,

413   respectively, via intraperitoneal injection of BLTL mice both prior to and after infection (**Fig. 9A**).

414   Human monocytes, as well as some macrophages and dendritic cells (DC) express CD4 (*49, 50*),

16

415   and the use of these three depleting antibodies will allow us to deconvolute the distinctive impact

416   of T-cells and monocytes in driving infection resolution.

417   Flow cytometry confirmed effective systemic depletion in the blood (**Fig. S6A**). All animals

418   were euthanized at 12 dpi to assess for the persistence of SARS-CoV-2 infection in fLX. While

419   depletion of CD3+, CD4+, and CD8+ cells induced persistent infection in some or most of the

420   animals, only CD4+ cell depletion (mean Log PFU/mg tissue = 2.37) resulted in a statistically

421   significant defect in infection resolution compared to all other experimental conditions (isotype,

422   OKT3, and OKT8-treated mice) (**Fig. 9B**). The rate of productively infected fLX was also higher

423   in CD4+ cell-depleted animals, with 72% of fLX (8/11) showing infection at 12 dpi compared to

424   50% (4/8) and 33% (2/6) in CD3- and CD8-depleted mice, respectively (**Fig. 9B**). Additionally,

425   when examining the average viral titer (Log PFU/mg of tissue) of persistently infected fLX, the

426   ones from CD4+ cell-depleted animals were significantly higher compared to CD3+ cell- depleted

427   fLX (**Fig. S6B**), furthering that CD4+ cells have a more consequential impact on driving infection

428   resolution than CD3+ cells. Anti-SARS-CoV-2 N IHC confirmed these findings and superior defect

429   of CD4+ cell-depleted animals to resolve infection (**Fig. 9C**). Using multiplex fluorescent IHC

430   (mIHC), we also validated the reduction in CD3+, CD4+ and CD3+ CD4- cells in fLX from CD3-,

431   CD4+ and CD8+ cell-depleted animals respectively, compared to isotype-treated animals

432   (**Fig.9D**). In the fLX of CD4+ cell-depleted mice, CD4+ cells depletion also associated with

433   significant reduction of CD163+ cells at 12 dpi, underscoring the association between CD4+

434   infiltration into fLX and CD163+ cell recruitment and differentiation (**Fig. 9E,F**).

435   Persistent infection in CD4+ cell-depleted animals was also associated with significant

436   downregulation of MHC class I (**Fig. 10**), a phenomenon we similarly observed in acutely infected

437   fLX (2 dpi) (**Fig. 10)** and that has been previously reported in cells with active SARS-CoV-2

438   replication (*51, 52*). This further emphasizes that depletion of CD4+ cells is associated with

439   defective viral clearance mechanisms. These findings suggest that circulating CD4-expressing

440   cells significantly mediate SARS-CoV-2 infection resolution in BLT-L mice.

441

Defective monocyte recruitment is associated with systemic and local signatures of chronic infection.

To further interrogate the impact of CD4+ depletion and monocyte recruitment on SARS-CoV-2 infection, we investigated fLX antiviral responses during acute and persistent infection by quantifying the concentration of 32 cytokines in the peripheral blood of naïve, acutely infected, persistently infected or recovered BLTL mice. Systemic levels of human CCL2 and CCL3, major monocyte attractants, were elevated in CD4+ cell-depleted mice and comparable to those of acutely infected mice (**Fig. 11A,B**). The maintenance of myeloid chemotaxis signals in persistently infected fLX further underlines the contribution of myeloid recruitment in SARS-CoV-2 infection resolution. Notably, among all cytokines and chemokines analyzed, CXCL10 was the only one displaying significantly increased serum levels in acutely infected mice (2 dpi) prior to returning to undetectable levels upon infection resolution (12 dpi) (**Fig 11C**). Several human subsets within fLX express *CXCL10* upon acute infection, including myeloid, mesenchymal and endothelial subsets (**Fig. 11D,E**). However, the myeloid compartment was the major source of *CXCL10* among all human clusters at 2 dpi (**Fig. 11D,E**) and this phenotype was dominantly driven by iMO (**Fig. 7G and 11E**). Therefore, our findings suggest an association between circulating human CXCL10 during acute infection and the simultaneous differentiation of iMO. Notably, levels of circulating human CXCL10 in persistently infected CD4+ cell-depleted mice were not statistically different than those of mice that resolved infection (12 dpi) (**Fig. 11C**). These results emphasize a link between persistent infection and lack of effective CXCL10 responses, further strengthening a connection between monocyte recruitment, iMO antiviral responses and SARS-CoV-2 infection resolution.

Persistently-infected mice antiviral responses were also distinguishable from acutely infected (2 dpi) and isotype-treated (12 dpi) mice by elevated levels of CCL19 in serum (**Fig. 11F**). CCL19 is a pro-inflammatory cytokine that has been linked with persistent viral replication and

18

467   inflammation such as in the context of HIV-1 infection (*53*), underlining that persistent SARS-CoV-

468   2 infection in BLT-L mice recapitulate key immunological features of chronic viral infection.

469   We have previously reported that fLX exhibit significant histopathological manifestations

470   of disease upon SARS-CoV-2 infection in the absence of an engrafted human immune system

471   (*3*), highlighting that tissue damage in fLX is virally induced. However, persistent infection did not

472   result in any significant histopathological manifestations of disease in fLX, which strongly

473   contrasts with acutely infected fLX (**Fig. 2H, Fig. 11G**). As minimal tissue damage is a hallmark

474   of chronic viral infection (*54*), these findings further support evidence that CD4+ cell depletion

475   promotes tissue remodeling processes underlying chronic infection and lasting viral persistence.

476

477   **DISCUSSION**

478   As our appreciation of the immunological differences between mice and humans continues

479   to grow, humanized mouse models increasingly stand out as robust platforms to understand how

480   viral pathogens interact with human tissues and the human immune system. These models are

481   especially valuable when investigating tissue and mucosal immunity since such investigations

482   remain impractical in human patients.

483   The SARS-CoV-2 pandemic has emphasized the need to increase our understanding of

484   immune mechanisms that can drive protection against immunologically novel respiratory viruses.

485   Mice engrafted with human immune systems and human lung tissues have emerged as valuable

486   tools for such investigations (*21, 23-25*), bridging the limitations of conventional animal models

487   and the challenges associated with human studies. We previously reported using the HNFL

488   mouse model that such models can be leveraged to capture immunological signatures defining

489   effective control of SARS-CoV-2 infection (*23*). However, the enhanced myeloid reconstitution of

490   the HNFL model rapidly inhibits viral replication in fLX, precluding our ability to study protective

491   naive immunological mechanisms at play upon acute and potentially symptomatic infection. This

492   study aimed to uncover novel facets of these mechanisms using a humanized mouse model that

19

493 exhibits robust susceptibility to acute SARS-CoV-2 infection prior resolving infection in a

494 hematopoietic-dependent manner.

495 We found that BTL-L mice are able to effectively clear infectious viral particles following

496 an early peak of viral replication in fLX. Infection resolution was associated with rapid mobilization

497 of the human immune cells into fLX upon viral inoculation, which aligns with previous evidence

498 that immunodeficient mice only engrafted with fLX are unable to clear infection (*22, 23*). Using

499 scRNAseq analysis, we identified a comprehensive network of novel factors involved in the

500 resolution of SARS-CoV-2 infection (**Fig. 12**). Our study identified three major hallmarks of this

501 process: 1) The recruitment of iMO, which display high level of enrichment in viral RNA and mount

502 dominant antiviral responses across all myeloid lineages, notably defined by CXCL10 expression;

503 2) The differentiation of mDNT cells, which are highly enriched in viral RNA and exhibit non-

504 canonical macrophage features and cytotoxic signatures; And 3) The synergistic contribution of

505 endothelial and mesenchymal cells in infection resolution via potentiating antiviral responses and

506 myeloid chemotaxis, respectively. Consistent with monocyte infiltration into infected fLX being a

507 dominant feature of our infection resolution model, systemic depletion of CD4+ cells, but not T-

508 cells, abrogated viral clearance. Persistent infection is associated with the lack of systemic

509 CXCL10 responses, dominantly mediated by iMO, as well as with signatures of chronic infection,

510 including systemic CCL19 expression and lack of fLX damage.

511 Our findings empower a recent human study reporting that protection from SARS-CoV-2

512 infection is associated with a rapid monocyte response in the nasal cavity and a decreased

513 number of circulating monocytes(*14*). Specifically, our work extends the findings of this human

514 study beyond the limitations of the human model by exploring tissue-resident events, unraveling

515 the identity of monocyte populations that extravasate tissues, differentiate and mount tissue-

516 resident immune responses to clear infection. By providing enhanced resolution on key protective

517 immunological processes and mediators that human studies alone cannot capture, our works

518   underscores how human and humanized mouse studies can effectively complement themselves

519   for improving our understanding of human antiviral immunity.

520

521   To the best of our knowledge, this study represents the initial evidence of a direct role

522   played by human lung extravascular inflammatory monocytes in the resolution of respiratory viral

523   infections. Extravascular monocytes have been proposed to serve as immune sentinels through

524   their position at the interface of the lung capillaries and alveoli (*55, 56*). However, although

525   previous research reported that these cells can promote T-cell resident memory differentiation

526   following viral infection (*57*), their direct antiviral functions have not been documented until now.

527   Four major features characterized these cells: 1) a dominant CD163-expressing population that

528   emerges during acute infection before dissipating, 2) a major source of CXCL10 expression, 3) a

529   high enrichment in viral RNA, and 4) the induction of robust antiviral responses.

530   Several lines of evidence support the monocyte nature of these cells. They display a close

531   transcriptomic relationship with patrolling monocytes, which have been reported to give rise to

532   transient, non-classical extravascular (including alveolar) monocytes in the mouse lung (*56*). The

533   iMO gene expression profile is also similar to those of human FCN1-monocytes recovered from

534   the broncho-alveolar lavage of COVID-19 patients with acute respiratory disease syndrome (*58*).

535   While further studies are needed, our data collectively suggest CD4+ PIM infiltrating the infected

536   fLX may differentiate into iMO to promote robust antiviral responses. Furthermore, our data show

537   that some iMO are negative for viral RNA, suggesting that such differentiation is independent of

538   an association with viral materials, although the presence of viral RNA could potentiate antiviral

539   responses.

540   The fate of iMO following infection resolution also remains unclear and will have to be

541   further deciphered. By 12 dpi and infection resolution, fLX display residual iMO and are enriched

542   in CD4+ PIM and CD163+ CD206+ IM. CD206+ IM are involved in response to wounding and

543   infection recovery (*56*) and CD163+ CD206+ monocyte-derived IM (*58*) have been shown to

544 directly derive from extravasating, circulating CD14+ monocytes in another human immune

545 system-engrafted mouse model (*59*). Therefore, one hypothesis would be that the pool of CD163+

546 CD206+ IM is derived both from iMO and newly recruited circulating monocytes.

547 Our findings also reveal that different monocytic fates are likely associated with distinct

548 clinical outcomes of SARS-CoV-2 infection. While our study emphasizes the protective role of

549 monocytes in preventing severe COVID-19, monocytic lineages have also been associated with

550 severe COVID-19(*2, 5, 36, 58*). Excessive monocyte infiltration, macrophage inflammation and

551 fibrotic response can lead to potentially fatal acute respiratory distress syndrome (ARDS) and

552 fibrosis despite promoting infection resolution. A suspected driver of excessive myeloid

553 inflammation is the ability of SARS-CoV-2 to trigger abortive infection of both monocytes and

554 macrophages(*27, 60-62*) through viral RNA replication and protein production, which results in

555 inflammasome activation(*27, 28, 63*). Consistently, viral RNA is enriched in inflammatory

556 monocytes and macrophages in lung autopsy samples from fatal COVID-19 cases (*5*). However,

557 our findings that viral RNA in iMO is associated with infection resolution and tissue protection

558 suggest that rapid clearance of viral RNA-enriched inflammatory monocytes, as opposed to their

559 persistence, is associated with favorable clinical outcomes.

560 Lung extravascular monocytes deriving from PIM also exhibit a dynamic transition state

561 and can differentiate into CD206- IM(*56*), primary responders to infection and important drivers of

562 inflammation. However, no CD206- macrophages were observed in infected fLX at any time point.

563 The transient presence of viral RNA-enriched iMO in fLX, leading to the absence of iMO

564 differentiation into CD206- IM, could therefore mitigate the risk of uncontrolled inflammation during

565 infection resolution. This process could prevent severe tissue damage and excessive

566 extravasation of circulating monocytes, which would otherwise differentiate into pro-fibrotic

567 CD163+ CD206+ IM, a major driver of ARDS(*58*).

568 Understanding the cellular and molecular players defining the fate of iMO upon exposure

569 to SARS-CoV-2 and how key regulatory crossroads in this subset may result in differential clinical

570   outcomes is of particular interest. Compounding immune dysregulations, such as elevated

571   inflammatory baseline and/or epigenetic imprinting related to innate immune training (*64*), may

572   hinder PIM and/or iMO's ability to adequately regulate their inflammatory responses in a timely

573   manner upon encountering viral materials or inflammatory clues. This could also favor extended

574   cell survival (NF-κB is both involved in inflammasome activation and cell survival (*65*)) and

575   subsequent differentiation into inflammatory macrophages, fostering exacerbated inflammation.

576   Our study also creates a mandate for probing the ubiquitous nature of iMO antiviral responses

577   during other respiratory viral infections and investigating more comprehensively the antiviral

578   functions of this novel subset beyond SARS-CoV-2 infection.

579

580   In parallel to ExiMO, we also identified mDNT cells, a transient DNT cell population highly

581   enriched in viral RNA and only observed upon acute infection, and which exhibits expression of

582   key macrophage-defining genes and cytotoxic markers. This population displays similarities with

583   a subpopulation of cytotoxic DNT cells previously reported in mouse spleen(*38*) and with innate-

584   like T-cells(*66*), which also harbor cytotoxic signatures. mDNT also share transcriptomic

585   similarities with γδ T-cell subsets previously described as bearing myeloid and cytotoxic

586   functions(*67, 68*). However, mDNT appear unique through a specific blend of lymphoid, and

587   conventional macrophage and mesenchymal markers and their short-lived nature (suggested by

588   their complete absence at 12 dpi). While CD8+ T-cells and macrophages isolated from

589   nasopharyngeal swabs have been identified to harbor SARS-CoV-2 RNA in human challenge

590   studies(*14*), mDNT did not meet the canonical transcriptomic signatures of these subsets,

591   suggesting the existence of tissue-resident events driving specific cellular differentiation

592   processes upon infection. Additional investigations are required to better understand the identity,

593   fate and functions of this cell subset in lung antiviral immunity. However, it is tempting to speculate

594   that mDNT may uniquely synergize CD8+ cytotoxic T-cell functions with viral particle phagocytosis

595   to effectively control infection prior to undergoing rapid cell death.

23

596   Despite our findings related to mDNT, the contribution of T-cells in SARS-CoV-2 infection

597   resolution remains elusive in our model. CD3+ cell depletion resulted in a partial abrogation of

598   infection resolution, with 50% of animals still capable of clearing infection. In addition, even when

599   viral infection persisted in CD3+ cell-depleted animals, viral titers in fLX remained significantly

600   lower than in the fLX of persistently infected CD4+ cell-depleted animals. One possible

601   interpretation is that T-cell depletion delays but does not abolish infection resolution. CD8+ cell-

602   depleted mice may display delayed viral clearance compared to isotype-treated mice (with

603   resolution occurring between 6dpi and 12 dpi), and CD3+ T-cell-depleted mice may be undergoing

604   progressive resolution by 12 dpi until complete clearance by a later time. In contrast, the viral titer

605   observed in fLX of CD4+ cell-depleted mice show no evidence of ongoing infection resolution.

606   How CD3+ depletion may impact mDNT differentiation, and how T-cells (including mDNT) and

607   ExiMO functions may synergize to rapidly resolve infection without extensive inflammation-

608   induced tissue damage will need further investigation.

609

610   There are inherent limitations associated with the BLT-L mouse model. First, direct viral

611   inoculation into fLX potentially bypasses key immune checkpoints in the upper respiratory tract,

612   which are not recapitulated in our model. Second, the hematopoietic reconstitution and functions

613   of the BLT-L mouse model remain imperfect, notably through the underrepresentation of specific

614   hematopoietic subsets, including dendritic cells and granulocytes, and limited B-cell responses –

615   which may ultimately bias the dynamics of viral clearance. Despite these limitations, BLT-L mice

616   recapitulated human lung responses to SARS-CoV-2 infection through AT2 loss of programming,

617   fibroblast and endothelial activation, and effective clearance of infection through robust

618   hematopoietic responses. This mouse model also supported viral adaptation processes with

619   public health relevance, and recapitulated signatures of persistent viral replication observed in

620   patients suffering from chronic infection. Our work demonstrates the potential of the BLT-L mouse

621   model to uncover naïve immune mechanisms and mediators governing the effective resolution of

622   lung infection by SARS-CoV-2 and open avenues for a comprehensive examination of such

623   processes against other viral respiratory infections, which may pave the way toward innovative

624   immunotherapy strategies against these diseases.

625

626   **AUTHOR CONTRIBUTIONS**

627   D.K., A.B.B. and F.D. conceptualized the overall study. C.H. conceptualized the computational

628   component of this study and oversaw the analysis of the single-cell RNA sequencing data. D.K.,

629   A.B.B., N.A.C. and F.D. designed the experiments. D.K., A.K.O., M.S, A.N, H.P.G., M.E., V.V.,

630   A.B.B. and F.D. performed experiments. D.K., A.K.O., A.T., J.T., M.S, A.N, P.M., M.E., J.H.C.,

631   V.V., N.A.C., C.H., A.B.B. and F.D. analyzed the data. J.T and C.H. carried out computational

632   analysis. M.E. carried out electron microscopy analysis. A.B.B. and V.V. provided access to key

633   resources. D.K. and F.D. wrote the manuscript with contributions from all authors.

634

25

657

658   **MATERIALS AND METHODS**

659   Detailed descriptions of the materials and methods used for this study are in the Supplemental

660   Materials.

661

662   ***Institutional approvals.*** All experiments in this study, including those conducted in BSL-3, were

663   approved by an institutional biosafety committee. Animal experiments described in this study were

664   performed in accordance with protocols that were reviewed and approved by the Institutional

665   Animal Care and Use and Committee of the Ragon Institution and Boston University. All mice

666   were maintained in facilities accredited by the Association for the Assessment and Accreditation

667   of Laboratory Animal Care (AAALAC). All replication-competent SARS-CoV-2 experiments were

668   performed in a biosafety level 3 laboratory (BSL-3) at the Boston University National Emerging

669   Infectious Diseases Laboratories (NEIDL).

670

671   ***Mouse strains and sex as biological variable.*** Female NOD.Cg.-$Prkdc^{Scid}Il2rg^{tm1Wjl}$/SzJ (NSG)

672   mice were obtained from the Jackson Laboratory, catalog number 005557. NSG mice were

673   maintained by the Ragon Institute Human Immune System Mouse core prior to engraftment and

674   shipment to the NEIDL, Boston University. In our study, only female mice were engrafted with

675   human fetal tissues because of their ability to support higher levels of engraftment than males.

676   As we investigated human tissue responses to infection and only leveraged mice as

677   xenorecipients, the sex of the animals does represent a critical variable for our study.

678

679   ***Human fetal tissues.*** De-identified human fetal tissues were procured from Advanced Bioscience

680   Resources (Alameda, CA, USA).

681

682   ***Generation of BLT-L mice.*** BLT mice were generated via irradiation of female NOD.Cg.-

683   *Prkdc^{Scid}Il2rg^{tm1Wjl}*/SzJ mice (NSG mice; Jackson Laboratory #005557) prior to implantation of

684   human fetal thymic and fetal liver tissue (Advanced Bioscience Resources) under the murine

685   kidney capsule. Two pieces of homologous human fetal lung tissue were implanted into

686   subcutaneous dorsal pockets of mice. Post-implantation, mice intravenously received 1×10^5

687   homologous CD34+ cells. Human immune reconstitution was determined by flow cytometry at

688   weeks post-implantation. Three distinct human donors were used for this study.

689

690   ***Mouse inoculation with SARS-CoV-2.*** BLT-L mice were anesthetized with 1–3% isoflurane prior

691   to inoculation via subcutaneous, intra-fetal lung xenograft (intra-fLX) injection with 10^6 plaque

692   forming unites (PFU) of SARS-CoV-2 WA-1 isolate in 50 µL of sterile 1X PBS. Mice were

693   euthanized at 2-, 6-, and 12-days post inoculation.

694

695   ***In vivo antibody depletion.*** BLT-L mice were administered 200 mg of anti-CD3e (OKT3)

696   (BioxCell; cat. # BE0001-2), anti-CD4 (OKT4) (BioxCell; cat. # BE0003-2), anti-CD8 (OKT8)

697   (BioxCell; cat. # BE0004-2), or isotype IgG2a (Thermofisher; cat # 02-6200) antibody 3-, 2-, and

698   1-day prior to inoculation and 4- and 8-days post inoculation with 1×10^6 PFU SARS-CoV-2 WA-

699   1.

700

Quantification and statistical Analysis. For histopathological score and viral load/titer comparisons a Kruskla-Wallis, non-parametric one-way ANOVA with Benjamini, Krieger, and Yekutieli correction for multiple comparisons was applied given the non-continuous nature of the data. For cytokine data, an Ordinary one-way ANOVA with uncorrected Fishers LSD was used as the data was collected from different time points, treatment conditions, and cohorts. A Kruskla-Wallis, non-parametric one-way ANOVA with an uncorrected Dunn's test was applied for CD163+ Area quantification (AQ) due to the independent comparisons between the samples. All statistical tests and graphical depictions of results were performed using GraphPad Prism version 9.0.1 software (GraphPad Software, La Jolla, CA). For all tests, p≤0.05 was considered statistically significant. Statistical significance on figures and supplemental figures is labeled with p-values and non-significant values are labeled with n.s. or left unlabeled.

712

Data availability. The Genome Expression Omnibus (GEO) accession number to access the raw data of our scRNAseq analysis is GSE255200.

715

REFERENCES

1. J. C. Melms *et al.*, A molecular single-cell lung atlas of lethal COVID-19. *Nature* **595**, 114-119 (2021).
2. A. F. Rendeiro *et al.*, The spatial landscape of lung pathology during COVID-19 progression. *Nature* **593**, 564-569 (2021).
3. E. Wauters *et al.*, Discriminating mild from critical COVID-19 by innate and adaptive immune single-cell profiling of bronchoalveolar lavages. *Cell Res* **31**, 272-290 (2021).
4. R. A. Grant *et al.*, Circuits between infected macrophages and T cells in SARS-CoV-2 pneumonia. *Nature* **590**, 635-641 (2021).
5. T. M. Delorey *et al.*, COVID-19 tissue atlases reveal SARS-CoV-2 pathology and cellular targets. *Nature*, (2021).
6. M. Liao *et al.*, Single-cell landscape of bronchoalveolar immune cells in patients with COVID-19. *Nat Med* **26**, 842-844 (2020).
7. X. Ren *et al.*, COVID-19 immune features revealed by a large-scale single-cell transcriptome atlas. *Cell* **184**, 5838 (2021).
8. P. A. Szabo *et al.*, Longitudinal profiling of respiratory and systemic immune responses reveals myeloid cell-driven lung inflammation in severe COVID-19. *Immunity* **54**, 797-814 e796 (2021).

9.   S. S. Batah, A. T. Fabro, Pulmonary pathology of ARDS in COVID-19: A pathological review for clinicians. *Respir Med* **176**, 106239 (2021).

10.   C. Fan *et al.*, Animal models for COVID-19: advances, gaps and perspectives. *Signal Transduct Target Ther* **7**, 220 (2022).

11.   E. Stephenson *et al.*, Single-cell multi-omics analysis of the immune response in COVID-19. *Nat Med* **27**, 904-916 (2021).

12.   X. Ren *et al.*, COVID-19 immune features revealed by a large-scale single-cell transcriptome atlas. *Cell* **184**, 1895-1913 e1819 (2021).

13.   R. Edahiro *et al.*, Single-cell analyses and host genetics highlight the role of innate immune cells in COVID-19 severity. *Nat Genet* **55**, 753-767 (2023).

14.   R. G. H. Lindeboom *et al.*, Human SARS-CoV-2 challenge uncovers local and systemic response dynamics. *Nature*, (2024).

15.   D. G. Augusto *et al.*, A common allele of HLA is associated with asymptomatic SARS-CoV-2 infection. *Nature* **620**, 128-136 (2023).

16.   C. G. K. Ziegler *et al.*, Impaired local intrinsic immunity to SARS-CoV-2 infection in severe COVID-19. *Cell* **184**, 4713-4733 e4722 (2021).

17.   M. Dugas *et al.*, Less severe course of COVID-19 is associated with elevated levels of antibodies against seasonal human coronaviruses OC43 and HKU1 (HCoV OC43, HCoV HKU1). *Int J Infect Dis* **105**, 304-306 (2021).

18.   M. Sagar *et al.*, Recent endemic coronavirus infection is associated with less-severe COVID-19. *J Clin Invest* **131**, (2021).

19.   K. Medetgul-Ernar, M. M. Davis, Standing on the shoulders of mice. *Immunity* **55**, 1343-1353 (2022).

20.   A. Rongvaux *et al.*, Human hemato-lymphoid system mice: current use and future potential for medicine. *Annu Rev Immunol* **31**, 635-674 (2013).

21.   A. Wahl *et al.*, Precision mouse models with expanded tropism for human pathogens. *Nat Biotechnol* **37**, 1163-1173 (2019).

22.   A. Wahl *et al.*, SARS-CoV-2 infection is effectively treated and prevented by EIDD-2801. *Nature* **591**, 451-457 (2021).

23.   D. J. Kenney *et al.*, Humanized mice reveal a macrophage-enriched gene signature defining human lung tissue protection during SARS-CoV-2 infection. *Cell Rep* **39**, 110714 (2022).

24.   Y. Di *et al.*, SARS-CoV-2 Variant-Specific Infectivity and Immune Profiles Are Detectable in a Humanized Lung Mouse Model. *Viruses* **14**, (2022).

25.   R. Sun *et al.*, Humanized mice for investigating SARS-CoV-2 lung infection and associated human immune responses. *Eur J Immunol* **52**, 1640-1647 (2022).

26.   L. Baena Carstens *et al.*, Lung Inflammasome Activation in SARS-CoV-2 Post-Mortem Biopsies. *Int J Mol Sci* **23**, (2022).

27.   C. Junqueira *et al.*, FcgammaR-mediated SARS-CoV-2 infection of monocytes activates inflammation. *Nature* **606**, 576-584 (2022).

28.   E. Sefik *et al.*, Inflammasome activation in infected macrophages drives COVID-19 pathology. *Nature* **606**, 585-593 (2022).

29.   PMDA, Xevudy for Intravenous Infusion 500 mg_GlaxoSmithKline K.K._Report on Special Approval for Emergency; https://www.pmda.go.jp/files/000245006.pdf. (2021).

30.   A. Fagre *et al.*, SARS-CoV-2 infection, neuropathogenesis and transmission among deer mice: Implications for spillback to New World rodents. *PLoS Pathog* **17**, e1009585 (2021).

31.   C. Harly, M. Cam, J. Kaye, A. Bhandoola, Development and differentiation of early innate lymphoid progenitors. *J Exp Med* **215**, 249-262 (2018).

32.   G. Pizzolato *et al.*, Single-cell RNA sequencing unveils the shared and the distinct cytotoxic hallmarks of human TCRVdelta1 and TCRVdelta2 gammadelta T lymphocytes. *Proc Natl Acad Sci U S A* **116**, 11906-11915 (2019).

785 33. Q. Zhao *et al.*, Lymphopenia is associated with severe coronavirus disease 2019 (COVID-
786   19) infections: A systemic review and meta-analysis. *Int J Infect Dis* **96**, 131-135 (2020).
787 34. S. Tavakolpour, T. Rakhshandehroo, E. X. Wei, M. Rashidian, Lymphopenia during the
788   COVID-19 infection: What it shows and what can be learned. *Immunol Lett* **225**, 31-32
789   (2020).
790 35. J. Huang *et al.*, SARS-CoV-2 Infection of Pluripotent Stem Cell-Derived Human Lung
791   Alveolar Type 2 Cells Elicits a Rapid Epithelial-Intrinsic Inflammatory Response. *Cell stem*
792   *cell* **27**, 962-+ (2020).
793 36. E. Wauters *et al.*, Discriminating mild from critical COVID-19 by innate and adaptive
794   immune single-cell profiling of bronchoalveolar lavages. *Cell Res* **31**, 272-290 (2021).
795 37. A. Wu, H. Song, Regulation of alveolar type 2 stem/progenitor cells in lung injury and
796   regeneration. *Acta Biochim Biophys Sin (Shanghai)* **52**, 716-722 (2020).
797 38. L. Yang *et al.*, Transcriptome landscape of double negative T cells by single-cell RNA
798   sequencing. *J Autoimmun* **121**, 102653 (2021).
799 39. T. M. Delorey *et al.*, A single-cell and spatial atlas of autopsy tissues reveals pathology
800   and cellular targets of SARS-CoV-2. *bioRxiv*, 2021.2002.2025.430130 (2021).
801 40. L. Fu, Z. Liu, Y. Liu, Fibrinogen-like protein 2 in inflammatory diseases: A future
802   therapeutic target. *Int Immunopharmacol* **116**, 109799 (2023).
803 41. Y. Takakura *et al.*, Mitochondrial protein C15ORF48 is a stress-independent inducer of
804   autophagy that regulates oxidative stress and autoimmunity. *Nat Commun* **15**, 953 (2024).
805 42. S. A. Clayton *et al.*, Inflammation causes remodeling of mitochondrial cytochrome c
806   oxidase mediated by the bifunctional gene C15orf48. *Sci Adv* **7**, eabl5182 (2021).
807 43. S. K. Gupta, P. G. Lysko, K. Pillarisetti, E. Ohlstein, J. M. Stadel, Chemokine receptors in
808   human endothelial cells. Functional expression of CXCR4 and its transcriptional regulation
809   by inflammatory cytokines. *J Biol Chem* **273**, 4282-4287 (1998).
810 44. A. S. Leroyer *et al.*, CD146 (Cluster of Differentiation 146). *Arterioscler Thromb Vasc Biol*
811   **39**, 1026-1033 (2019).
812 45. H. M. Otifi, B. K. Adiga, Endothelial Dysfunction in Covid-19 Infection. *Am J Med Sci* **363**,
813   281-287 (2022).
814 46. Z. Qin *et al.*, Endothelial cell infection and dysfunction, immune activation in severe
815   COVID-19. *Theranostics* **11**, 8076-8091 (2021).
816 47. T. Kadiyska *et al.*, Role of endothelial dysfunction in the severity of COVID-19 infection
817   (Review). *Molecular medicine reports* **26**, (2022).
818 48. S. W. Xu, I. Ilyas, J. P. Weng, Endothelial dysfunction in COVID-19: an overview of
819   evidence, biomarkers, mechanisms and potential therapies. *Acta Pharmacol Sin* **44**, 695-
820   709 (2023).
821 49. A. Zhen *et al.*, CD4 ligation on human blood monocytes triggers macrophage
822   differentiation and enhances HIV infection. *J Virol* **88**, 9934-9946 (2014).
823 50. L. Jardine *et al.*, Rapid detection of dendritic cell and monocyte disorders using CD4 as a
824   lineage marker of the human peripheral blood antigen-presenting cell compartment. *Front*
825   *Immunol* **4**, 495 (2013).
826 51. N. Arshad *et al.*, SARS-CoV-2 accessory proteins ORF7a and ORF3a use distinct
827   mechanisms to down-regulate MHC-I surface expression. *Proc Natl Acad Sci U S A* **120**,
828   e2208525120 (2023).
829 52. J. S. Yoo *et al.*, SARS-CoV-2 inhibits induction of the MHC class I pathway by targeting
830   the STAT1-IRF1-NLRC5 axis. *Nat Commun* **12**, 6602 (2021).
831 53. J. K. Damas *et al.*, Homeostatic chemokines CCL19 and CCL21 promote inflammation in
832   human immunodeficiency virus-infected patients with ongoing viral replication. *Clin Exp*
833   *Immunol* **157**, 400-407 (2009).
834 54. E. I. Zuniga, M. Macal, G. M. Lewis, J. A. Harker, Innate and Adaptive Immune Regulation
835   During Chronic Viral Infections. *Annu Rev Virol* **2**, 573-597 (2015).

55. M. P. Rodero *et al.*, Immune surveillance of the lung by migrating tissue monocytes. *Elife* **4**, e07847 (2015).

56. J. Schyns *et al.*, Non-classical tissue monocytes and two functionally distinct populations of interstitial macrophages populate the mouse lung. *Nat Commun* **10**, 3964 (2019).

57. P. R. Dunbar *et al.*, Pulmonary monocytes interact with effector T cells in the lung tissue to drive T(RM) differentiation following viral infection. *Mucosal Immunol* **13**, 161-171 (2020).

58. D. Wendisch *et al.*, SARS-CoV-2 infection triggers profibrotic macrophage responses and lung fibrosis. *Cell* **184**, 6243-6261 e6227 (2021).

59. E. Evren *et al.*, Distinct developmental pathways from blood monocytes generate human lung macrophage diversity. *Immunity* **54**, 259-275 e257 (2021).

60. J. Zheng *et al.*, Severe Acute Respiratory Syndrome Coronavirus 2-Induced Immune Activation and Death of Monocyte-Derived Human Macrophages and Dendritic Cells. *J Infect Dis* **223**, 785-795 (2021).

61. A. Boumaza *et al.*, Monocytes and Macrophages, Targets of Severe Acute Respiratory Syndrome Coronavirus 2: The Clue for Coronavirus Disease 2019 Immunoparalysis. *J Infect Dis* **224**, 395-406 (2021).

62. D. Yang *et al.*, Attenuated Interferon and Proinflammatory Response in SARS-CoV-2-Infected Human Dendritic Cells Is Associated With Viral Antagonism of STAT1 Phosphorylation. *J Infect Dis* **222**, 734-745 (2020).

63. D. Munnur *et al.*, Altered ISGylation drives aberrant macrophage-dependent immune responses during SARS-CoV-2 infection. *Nat Immunol* **22**, 1416-1427 (2021).

64. J. Ochando, W. J. M. Mulder, J. C. Madsen, M. G. Netea, R. Duivenvoorden, Trained immunity - basic concepts and contributions to immunopathology. *Nat Rev Nephrol* **19**, 23-37 (2023).

65. M. Mussbacher, M. Derler, J. Basilio, J. A. Schmid, NF-kappaB in monocytes and macrophages - an inflammatory master regulator in multitalented immune cells. *Front Immunol* **14**, 1134661 (2023).

66. M. Molgora, M. Colonna, Innate-like T cells: A promising asset in anti-cancer immunity. *Cancer Cell* **40**, 714-716 (2022).

67. M. Lebedev, B. Faburay, J. A. Richt, A. Young, Myeloid-like gammadelta T cell subset in the immune response to an experimental Rift Valley fever vaccine in sheep. *Vet Immunol Immunopathol* **233**, 110184 (2021).

68. M. Muto, M. Baghdadi, R. Maekawa, H. Wada, K. Seino, Myeloid molecular characteristics of human gammadelta T cells support their acquisition of tumor antigen-presenting capacity. *Cancer Immunol Immunother* **64**, 941-949 (2015).
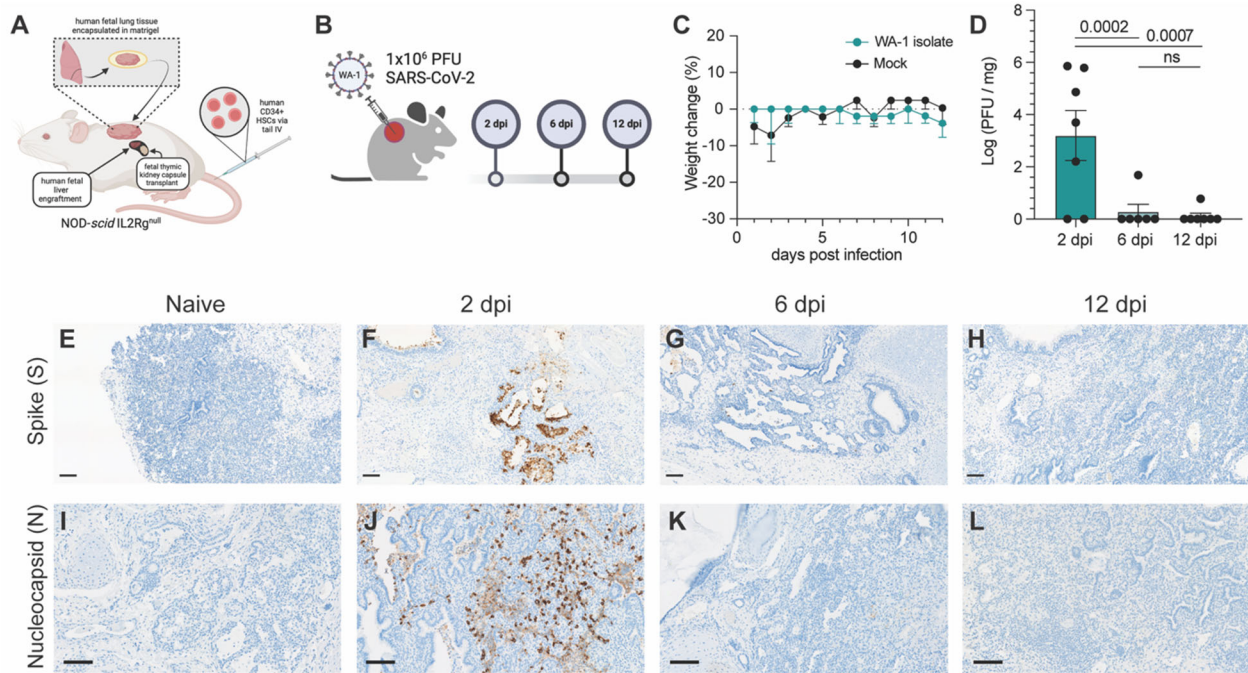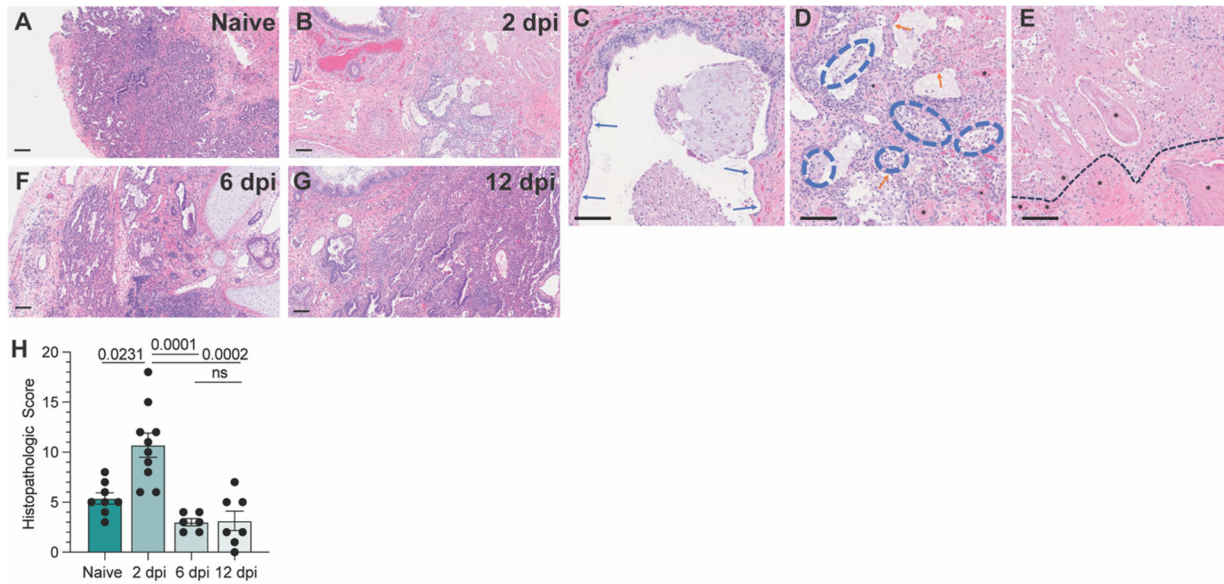
FIGURES

Figure 1. BLT-L mice effectively resolve SARS-CoV-2 infection. (A) Representative schematic of BLT-L mice. **(B)** Fetal lung xenografts (fLX) of BLT-L mice were infected with 1×10^6 PFU of SARS-CoV-2 WA-1 isolate via subcutaneous intra-graft injection. **(C)** BLT-L mice were monitored for weight change over the course of 12 days post-infection (dpi). **(D)** Viral titer (log(PFU/mg)) in fLX at 2, 6, and 12 dpi as determined by plaque assay. **(E-H)** Immunohistochemistry for SARS-CoV-2 S and **(I-L)** N protein were performed on naïve fLX **(E,I)** and fLX at 2 dpi **(F,J)**, 6dpi **(G,K),** and 12 dpi **(H,L)**. Scale bar = 100 μM. Data are representative of two or three independent experiments. n = 6 -10 per timepoint. Error bars represent mean ± standard error of the mean. *One-way ANOVA analysis was performed. p-values are indicated. n.s. = non-significant.*

32

Figure 2. BLT-L mice resolve histopathological damage in fLX. (A-E) Hematoxylin and eosin staining was performed on naïve fLX **(A)** and fLX at 2 dpi **(B-E)**, 6dpi **(F),** and 12 dpi **(G)**. Scale bar = 100 μM. **(C)** Bronchiolar attenuation and denuding (blue arrows) correlates directly with the presence of SARS-CoV-2 Spike protein. **(D)** Alveolar spaces are multifocally filled with necrotic debris admixed with neutrophils and edema (blue hashes). Type II pneumocytes (ATII) are often denuded or attenuated in areas of inflammation that correlates directly with the presence of SARS-CoV-2 Spike protein. Fibrin thrombi are routinely observed in neighboring parenchyma (black asterisks). **(E)** Coagulative necrosis as evidenced by loss of cellular detail and generalized eosinophilia (above the black hashed line) with numerous regional fibrin thrombi (black asterisks). Although SARS-CoV-2 Spike protein is not observed in the area of coagulative necrosis viral antigen is located within adjacent tissue. **(H)** Histopathological scoring of naïve fLX and fLX at 2, 6, and 12 dpi. Data are representative of two or three independent experiments. n = 6 -10 per timepoint. Error bars represent mean ± standard error of the mean. *One-way ANOVA analysis was performed. p-values are indicated. n.s. = non-significant.*

33
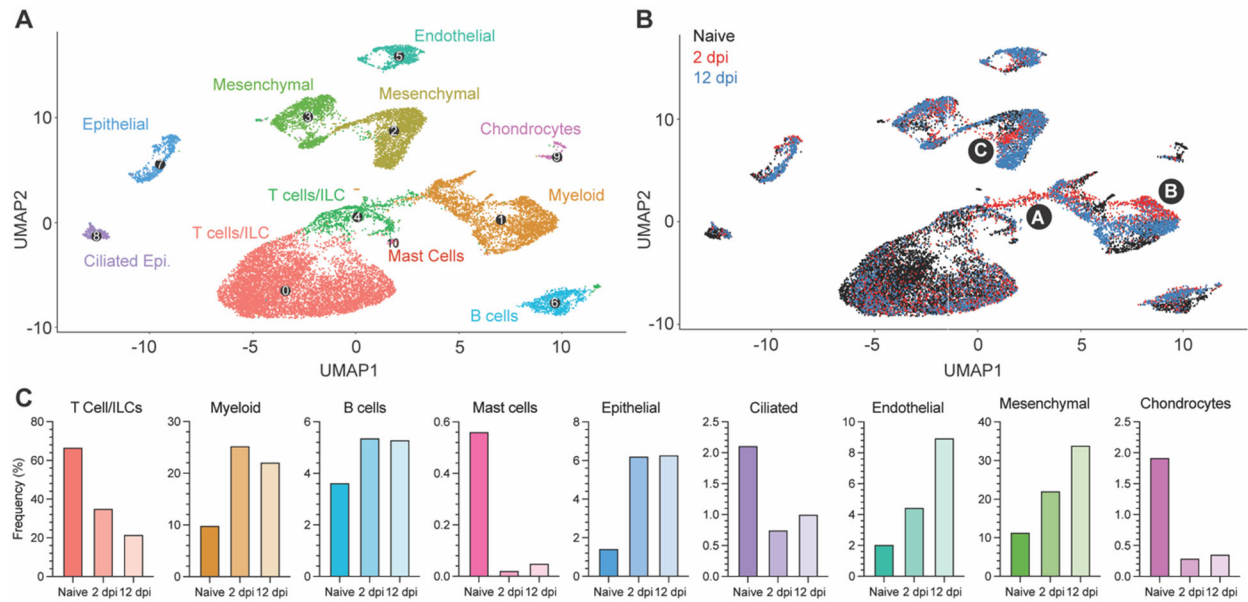
Figure 3. **Cellular remodeling and viral dynamics in fLX upon SARS-CoV-2 infection**

Single cell RNA sequencing analysis was performed on single cell suspensions of naïve fLX and fLX at 2 and 12 dpi. Naïve n=3 fLX (9,605 cells), 2 dpi n=2 fLX (4,405 cells), and 12 dpi n = 2 fLX (5,857 cells). **(A)** UMAP plot clustering of the human cell compartment of naïve fLX and fLX at 2 and 12 dpi. **(B)** Temporal annotation of the human clusters on the UMAP plot: naïve (black), 2 dpi (red), 12 dpi (blue). Sub-clusters unique to 2 dpi are annotated by A (T cell compartment), B (myeloid compartment) and C (mesenchymal compartment). **(C)** Frequency of each cell compartment determined by single cell RNA-sequencing.

925
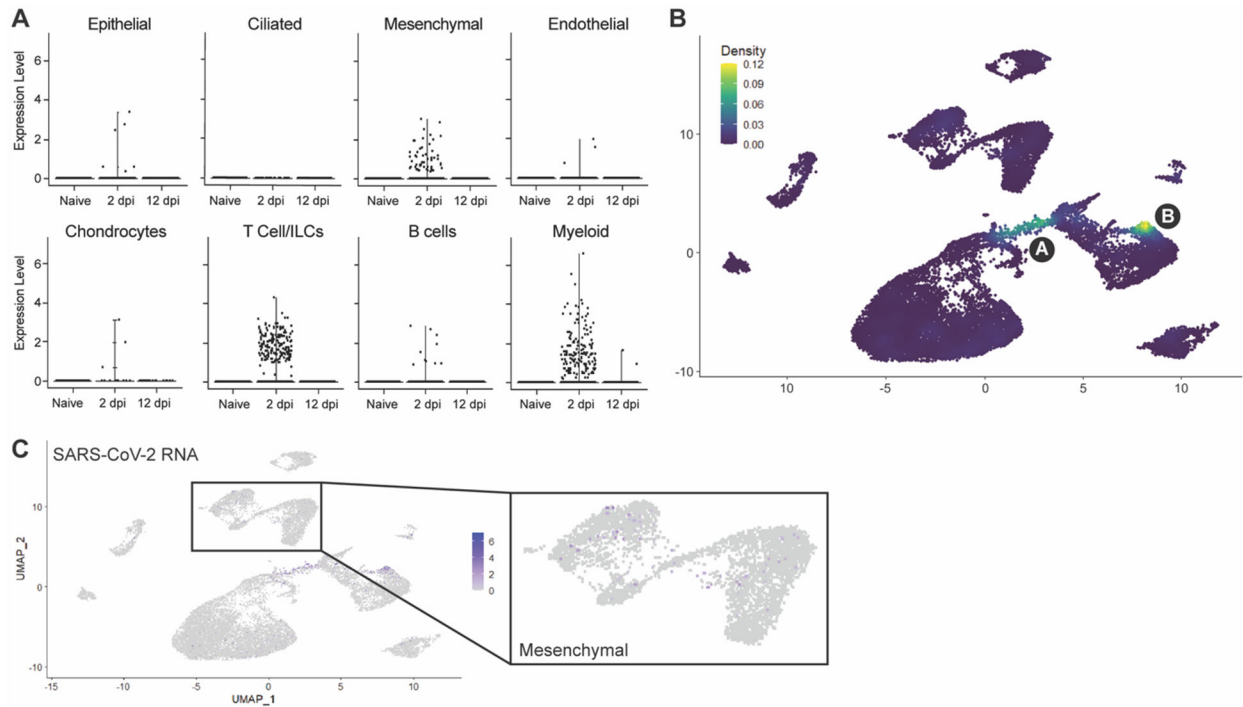
Figure 4. Cellular compartmentalization of viral RNA during infection. (A) Dot plots displaying the expression of SARS-CoV-2 viral RNA transcripts identified in scRNA-seq. **(B)** UMAP plot showing the distribution of SARS-CoV-2 viral RNA transcripts by density across all human cell clusters and time points. **(C)** UMAP plot showing the distribution of SARS-CoV-2 viral RNA reads across all human cell clusters and time points. Inset showing distribution of viral RNA reads in the mesenchymal cluster.

932

933

934

935

936

937

938
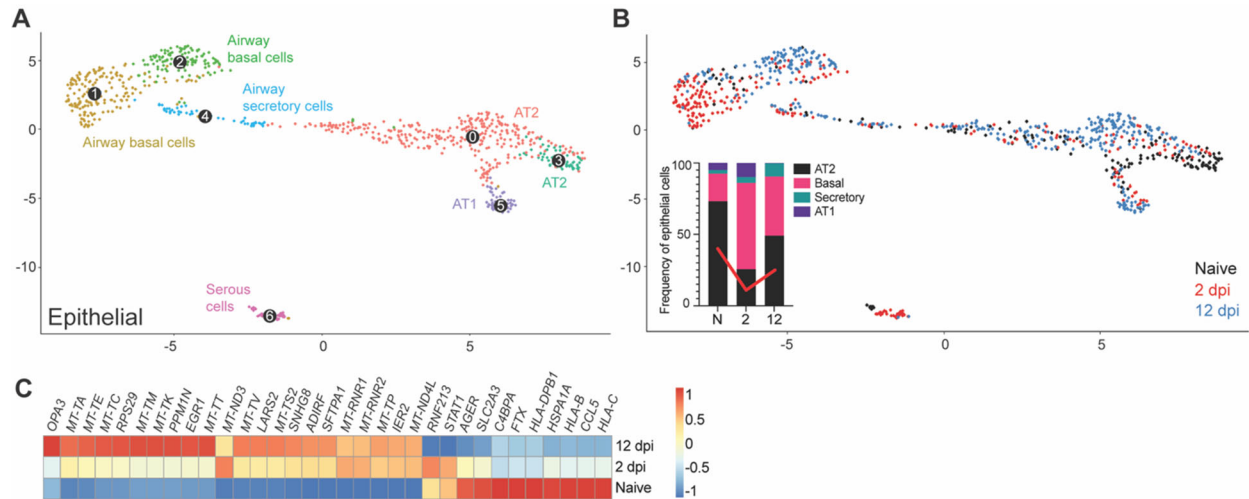
Figure 5. Remodeling of the epithelial compartment of fLX during infection. (A) UMAP plot sub-clustering of the human epithelial compartment in fLX across all time points. **(B)** Temporal annotation of the human epithelial sub-clusters on the UMAP plot: naïve (black), 2 dpi (red), 12 dpi (blue). The inset graph indicates the change in frequency of each compartment (AT2; black, Basal; pink, Secretory; teal, and AT1; purple) within the epithelial compartment. Red line indicates the change in the AT2 compartment over time. **(C)** Heatmap displaying the relative expression (from -1 to 1) of the top differentially regulated genes over the course of infection within the AT2 compartment.
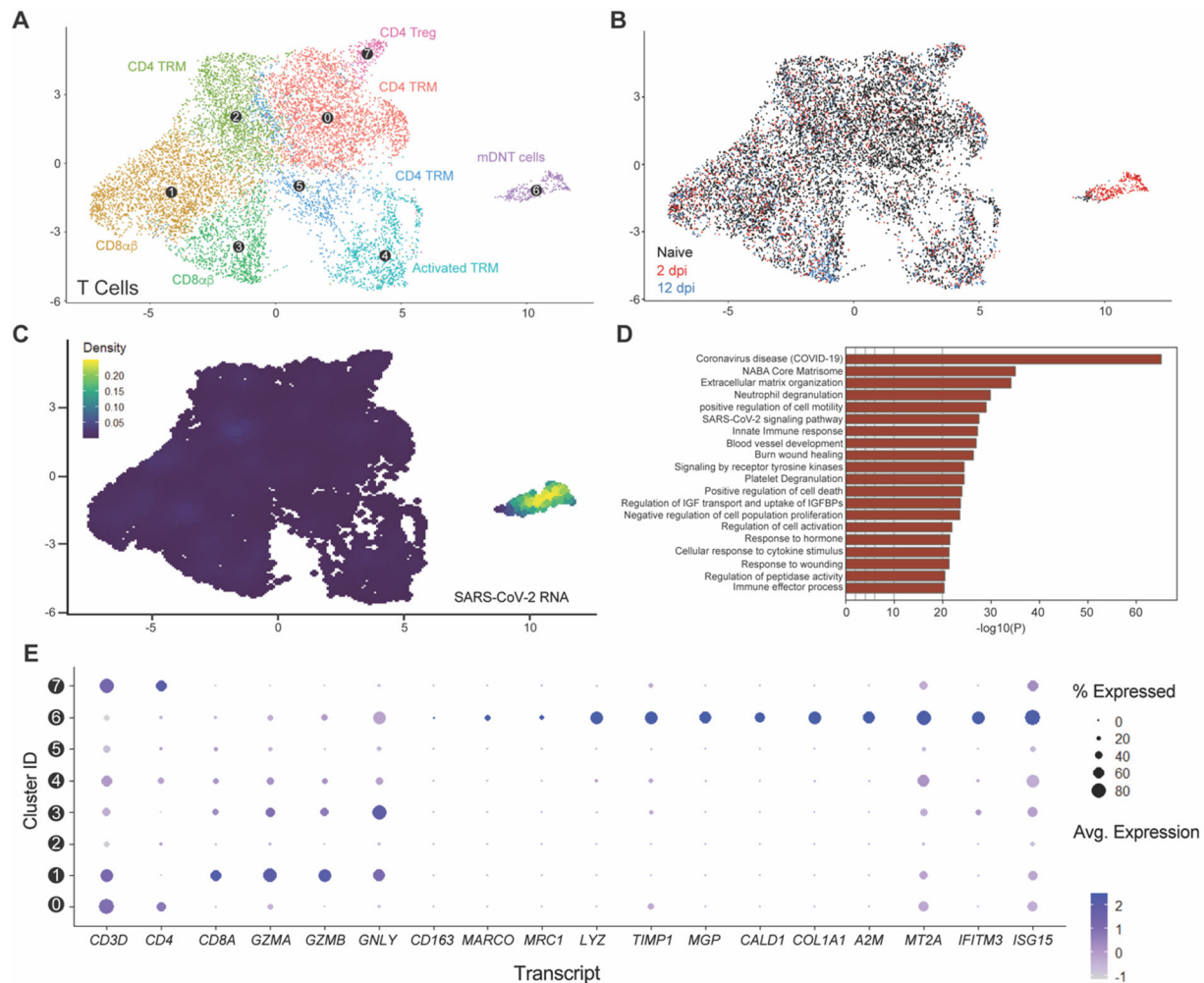
957

958

Figure 6. Myeloid-like double-negative T-cell emerges upon acute infection and are enriched in viral RNA. (A) UMAP plot showing the sub-clustering of the human T-cell compartment of fLX across all time points. **(B)** Temporal annotation of the human T-cell sub-clusters on the UMAP plot: naïve (black), 2 dpi (red),2 dpi (blue). **(C)** UMAP plot (all time points) showing the distribution of SARS-CoV-2 viral RNA transcripts in the T-cell compartment. **(D)** Go-term analysis showing the most highly upregulated signaling pathways in the mDNT (sub-cluster 6). **(E)** Relative expression of T cells, macrophage, mesenchymal and antiviral markers within each of the T-cell sub-clusters (From 0 to 7; as labeled in panel A).

967
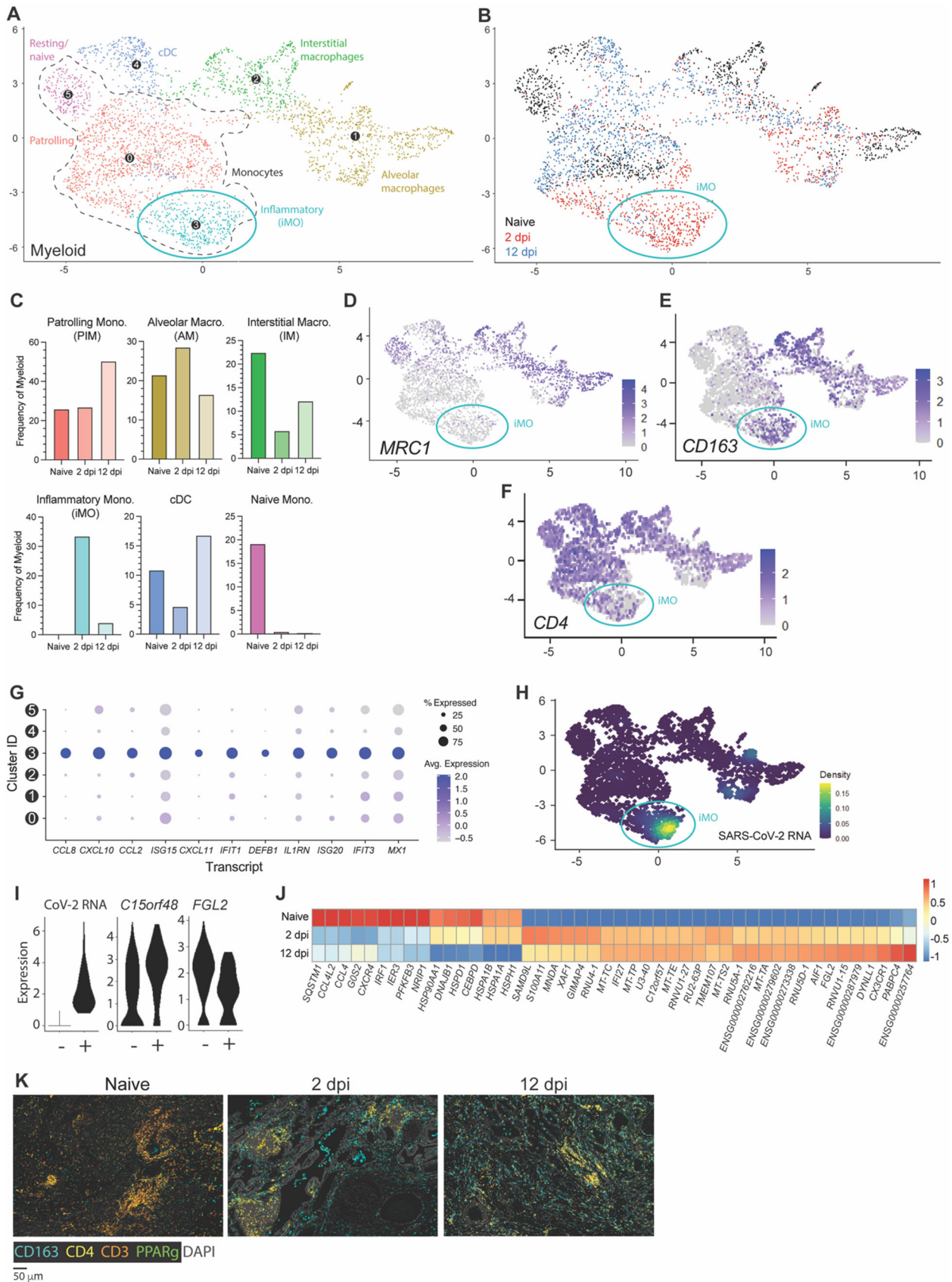
Figure 7. CD163+ extravascular inflammatory monocytes arise during acute viral infection and are predominant antiviral mediators. (A) UMAP plot showing sub-clustering of the human myeloid compartment of fLX across all time points. **(B)** Temporal annotation of the myeloid sub-clusters on the UMAP plot: naïve (black), 2 dpi (red), 12 dpi (blue). iMO sub-cluster is indicated with a blue circle. **(C)** Frequency of each myeloid sub-cluster by timepoint. **(D-F)** UMAP plot showing the expression of *MRC1* **(D)**, CD*163* **(E)**, and *CD4* **(F)** across myeloid sub-sets. **(G)** Relative expression of highly upregulated ISGs and inflammatory markers in each of the myeloid sub-clusters. **(H)** UMAP plot (all time points) showing the distribution of SARS-CoV-2 viral RNA transcripts in the myeloid compartment. **(I)** Violin plots showing expression level of differentially expressed genes between SARS-CoV-2 positive and negative ExiMO (sub-cluster 3). **(J)** Heatmap displaying the relative expression (from -1 to 1) of the top differentially regulated genes over the course of infection within the patrolling monocyte (0) compartment. **(K)** Multiplex fluorescent immunohistochemistry of naïve fLX and fLX at 2 and 12 dpi. CD163: teal, CD4: yellow, CD3: orange, PPARγ: green, Dapi: gray. Two representative images. Scale bar = 100 μM.

983

984

985 **Figure 8. (A)** UMAP plot sub-clustering of the human mesenchymal compartment in fLX across

986 all time points. **(B)** Temporal annotation of the mesenchymal sub-clusters on the UMAP plot:

987 naïve (black), 2 dpi (red), 12 dpi (blue). **(C)** Frequency of mesenchymal sub-clusters. **(D)** Go-term

988 analysis showing cellular pathways linked to significantly upregulated genes within the activated

40

989   fibroblasts sub-cluster. **(E-F)** UMAP plot showing *CXCL10* **(E)** and *TIMP1* **(F)** expression within

990   all human mesenchymal sub-clusters and across all time points. Activated fibroblasts are

991   indicated by a red circle in A and B. **(G)** UMAP plot sub-clustering of the human endothelial

992   compartment of fLX across all time points. **(H)** Temporal annotation of the endothelial sub-clusters

993   on the UMAP plot: naïve (black), 2 dpi (red), 12 dpi (blue). **(I)** List of upregulated (red) and

994   downregulated (blue) genes specific to the activated endothelial sub-cluster (Cluster 2) over the

995   other endothelial sub-clusters (*p.adj*≤0.05). **(J)** Heatmap displaying the relative expression (from

996   -1 to 1) of the top differentially regulated genes over the course of infection within the venous

997   endothelial compartment.

998

999

1000

1001

1002

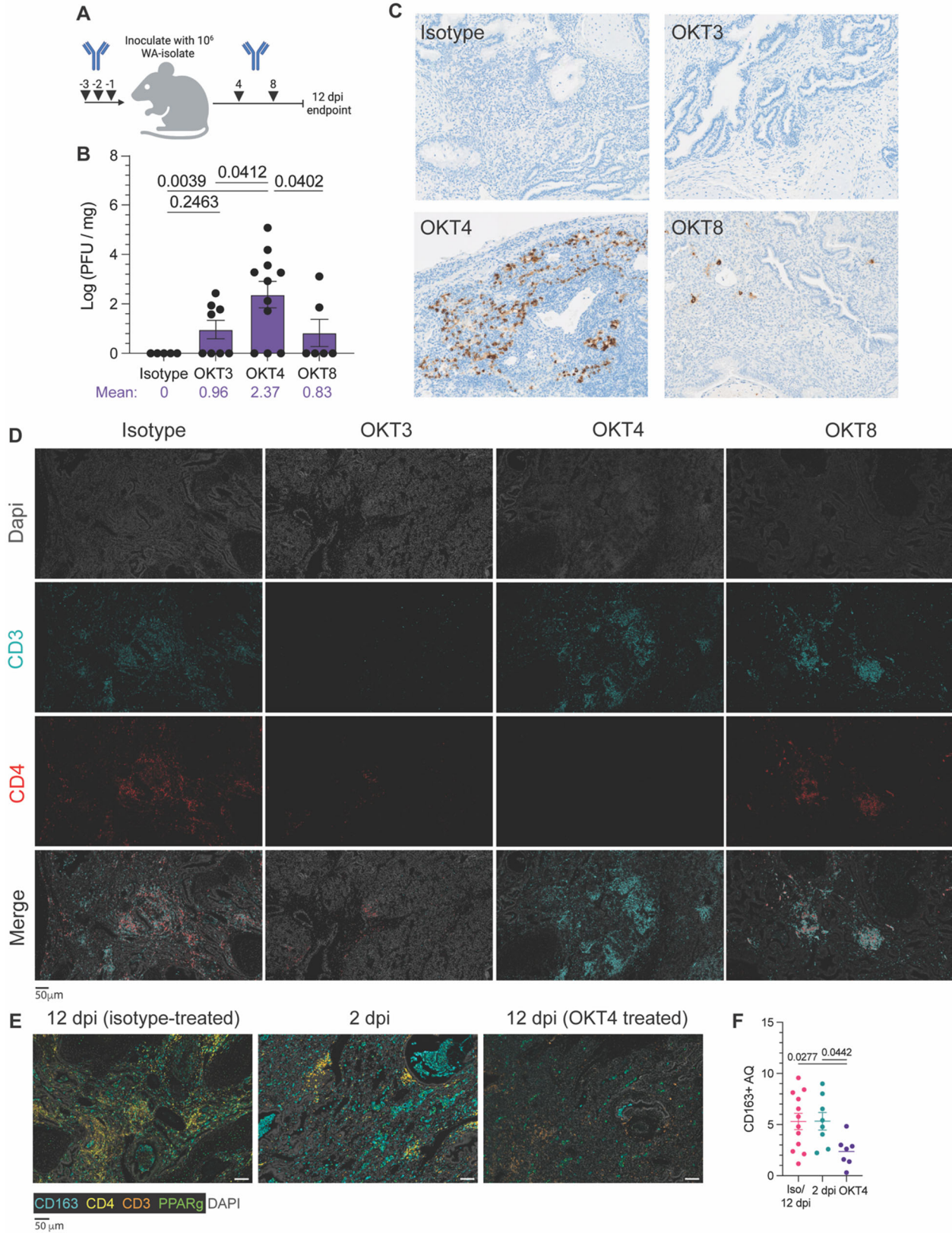1003

1004

1005

1006

1007

1008

1009

1010

1011

1012

1013

1014

Figure 9. Systemic depletion of CD4+ cells results in persistent infection of fLX. (A) BLT-L mice were administered 200 μg of anti-CD3e (OKT3), anti-CD4 (OKT4), anti-CD8 (OKT8) or IgG2a isotype. **(B)** Viral titer (log(PFU/mg)) in fLX extracted from BLT-L mice treated with isotype, OKT3, OKT4, or OKT8 antibody at 12 dpi. **(C)** Immunohistochemistry for SARS-CoV-2 N protein on fLX of depleted or non-depleted BLT-L mice at 12 dpi. **(D)** Multiplex immunohistochemistry on fLX of depleted or non-depleted BLT-L mice at 12 dpi. Dapi = gray, CD3 = teal, CD4 = red. Scale bar = 50 μm. **(E-F)** Multiplex fluorescent immunohistochemistry (E) and CD163+ area quantification (AQ) (F) of fLX that resolved infection (12 dpi, isotype treated), or eliciting acute (2 dpi) or persistent infection (12 dpi, OKT4 treated). CD163: teal, CD4: yellow, CD3: orange, PPARγ: green, Dapi: gray. Scale bar = 50 μM.
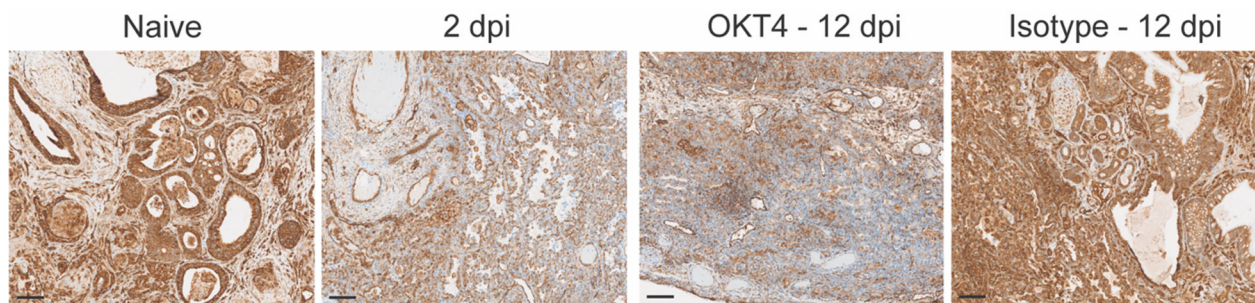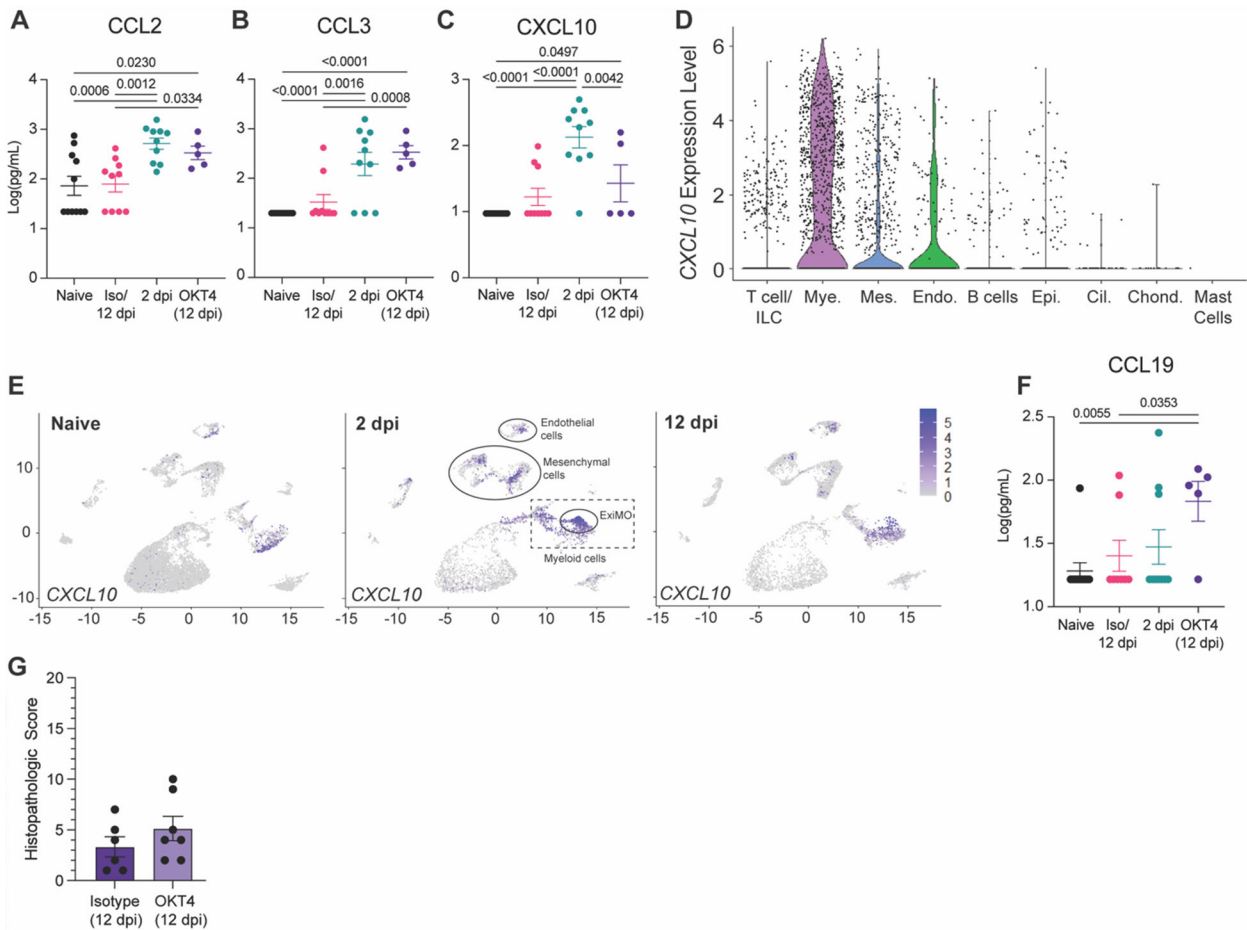

Figure 10. MHC-I staining of fLX tissue sections (anti-MHC class I (EMR8-5) CST 88274) extracted from naïve mice, OKT4-treated mice (12 dpi), or from infected fLX at 2 and 12 dpi. Scale bar = 100 μM

Figure 11. CD4+ cell depletion results in signatures of chronic infection. (A-C) Cytokine quantification (**A**: CCL2, **B**: CCL3, **C**: CXCL10) in the serum of naïve, infected (2 dpi and 12 dpi isotype-treated or not) and OKT4-treated BLT-L mice (12 dpi). **(D)** Violin plot showing expression level of *CXCL10* per cell and within each human lineage. **(E)** UMAP plot showing *CXCL10* expression within all human lineages in naive fLX and at 2- and 12 dpi. Locations of the mesenchymal, endothelial, myeloid and ExiMO clusters at 2 dpi are indicated. **(F)** Quantification of CCL19 in the serum of naïve, infected (2 dpi and 12 dpi isotype-treated or not) and OKT4-treated BLT-L mice (12 dpi). **(G)** Histopathological scoring of fLX extracted from isotype and OKT4-depleted BLT-L mice (12 dpi). Error bars indicate mean ± Standard error of the mean. One-*way ANOVA, t-test. p-values are indicated on graphs.*

44
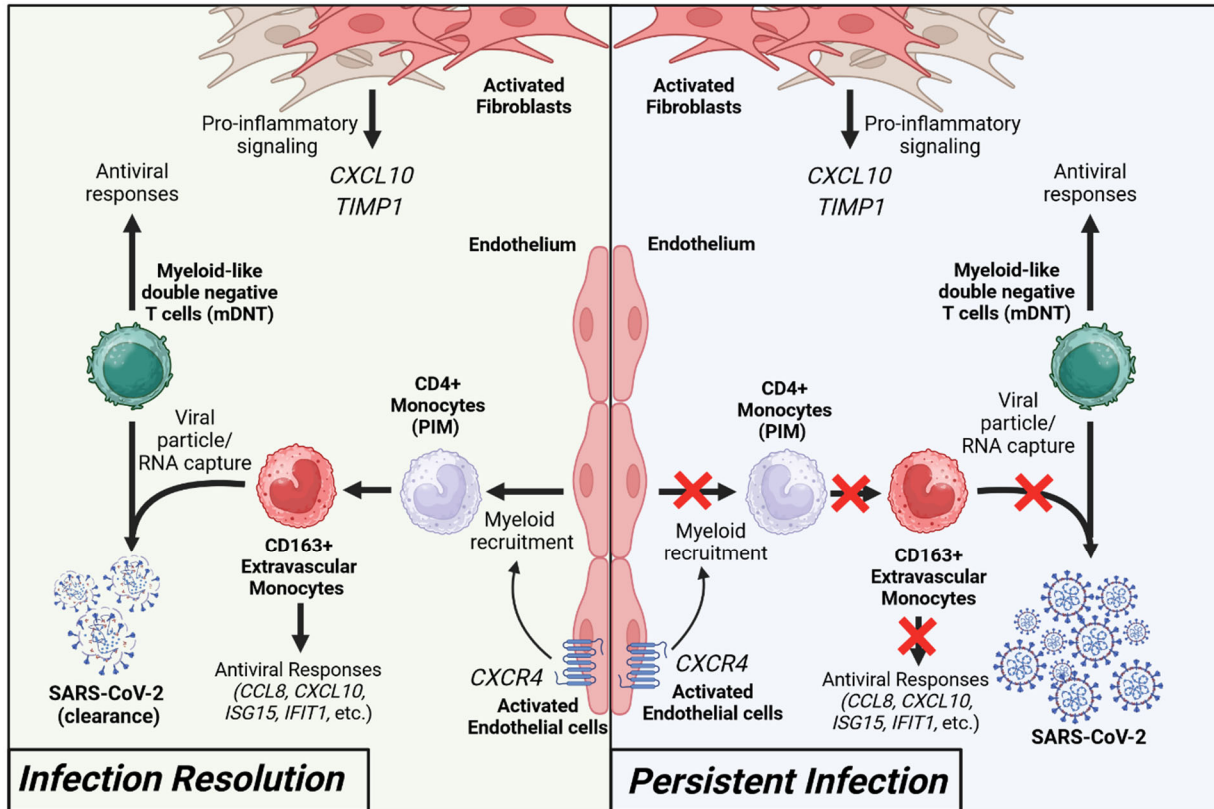
Figure 12. Immune signatures of SARS-CoV-2 infection resolution in human lung tissues. During effective viral resolution and tissue repair (left panel), myeloid cells are recruited to the site of infection and differentiates into CD163+ inflammatory monocytes (iMO). iMO produce antiviral and inflammatory signals and capture viral RNA/particles. Additionally, myeloid-like double negative T cells (mDNT), act to enhance the capture of viral RNA/particles and antiviral responses. In parallel, activated endothelial cells and fibroblasts contribute to the recruitment of myeloid cells and inflammatory response, respectively. Collectively, these events lead to viral clearance and infection resolution. In the context of persistent infection (left panel), absence of effective CD4+ monocyte recruitment prevents infection resolution.